FINAL REPORT

U. S. DEPARTMENT OF ENERGY

"IN-SITU" SPECTRO-ELECTROCHEMICAL STUDIES OF RADIONUCLIDE-CONTAMINATED SURFACE FILMS ON METALS

Principal Investigator:
Carlos A. Melendres
Argonne National Laboratory
Chemical Technology Division
Argonne, IL 60439

Collaborators:
Susan Mini
Northern Illinois University
Physics Department
DeKalb, IL 60115

Azzam N. Mansour
Naval Surface Warfare Center
Carderock Division
Bethesda, MD 20817

Project Number: 55380
Grant Number: W-31-109-ENG-38
Grant Project Officer: Chet Miller
Project Duration: October 1996 –September 1999

TABLE OF CONTENTS

EXECUTIVE SUMMARY

The incorporation of heavy metal ions and radioactive contaminants into hydrous oxide films has been investigated in order to provide fundamental knowledge that could lead to the technological development of cost-effective processes and techniques for the decontamination of storage tanks, piping systems, surfaces, etc, in DOE nuclear facilities. The formation of oxide/hydroxide films was simulated by electrodeposition onto a graphite substrate from solutions of the appropriate metal salt. Synchrotron X-ray Absorption Spectroscopy (XAS), supplemented by Laser Raman Spectroscopy (LRS), was used to determine the structure and composition of the host oxide film, as well as the impurity ion. Results have been obtained for the incorporation of Ce, Sr, Cr, Fe, and U into hydrous nickel oxide films. Ce and Sr oxides/hydroxides are co-precipitated with the nickel oxides in separate phase domains. Cr and Fe, on the other hand, are able to substitute into Ni lattice sites or intercalate in the interlamellar positions of the brucite structure of $Ni(OH)_2$. U was found to co-deposit as a U(VI) hydroxide. The mode of incorporation of metal ions depends both on the size and charge of the metal ion. The structure of iron oxide (hydroxide) films prepared by both anodic and cathodic deposition has also been extensively studied. The structure of $Fe(OH)_2$ was determined to be similar to that of α-$Ni(OH)_2$. Anodic deposition from solutions containing Fe^{2+} results in a film with a structure similar to γ-FeOOH. From the knowledge gained from the present studies, principles and methods for decontamination have become apparent. Contaminants sorbed on oxide surfaces or co-precipitated may be removed by acid wash and selective dissolution or complexation. Ions incorporated into lattice sites and interlamellar layers will require more drastic cleaning procedures. Electropolishing and the use of an "electrochemical brush" are among concepts that should be considered seriously for the latter cases. The incorporation of radionuclides into the structure of highly defective, insoluble oxides and clays should be considered for long-term storage and disposal. The establishment of a truly long-term (10 to 20 years) basic program on environmental science by DOE is strongly recommended. Avenues for future work are suggested.

RESEARCH OBJECTIVE

The objective of this research program was to gain a fundamental understanding of the structure, composition, and mechanism of formation of radionuclide-containing surface films on metals that are relevant to the problem of decontamination of piping systems and waste storage tanks at DOE nuclear facilities. The project sought to expand our knowledge, while obtaining useful practical information, through the conduct of systematic research that utilized the unique facilities at various synchrotron radiation sources for carrying out X-ray Absorption Spectroscopy (XAS). Among such sources are the Advanced Photon Source (APS) at Argonne National Laboratory, the National Synchrotron Light Source (NSLS) at Brookhaven National Laboratory, and the Stanford Synchrotron Radiation Laboratory (SSRL) at Stanford University. Work was carried out in collaboration with Northern Illinois University to ensure that a strong basic approach was taken in the analyses and the methodologies used to achieve the desired goals. In addition, in order to facilitate dissemination of the results and transfer technology that ensues from the project, contacts with prospective users were made, and collaboration was carried out with scientific personnel from a defense laboratory, the Naval Surface Warfare Center, which has interest in similar environmental problems.

METHODS

Radioactive contamination is often trapped in the corrosion scales that form on metal surfaces over long periods of service. An understanding of the local structure of heavy metal ions incorporated in such films is essential to developing cost-effective decontamination procedures for their cleanup via chemical and electrochemical techniques [1]. By incorporation is meant here any one of the following processes: co-precipitation, lattice substitution into vacancies or interstitial sites, intercalation, surface adsorption, or absorption in pores that ultimately results in the co-deposition of the impurity atom with the oxide film on a surface. The energetics of decontamination will likely depend on the nature of incorporation, i.e., a heavy metal ion in a lattice vacancy or interlamellar site would be more difficult to remove than one which is adsorbed on the surface. Of particular interest are the surface films on base metals such as iron, nickel, and chromium, which are the main constituents of stainless and carbon steels that are often used in piping systems and waste storage tanks. Work carried out in this

project involved: (1) simulation of the surface oxide films on Ni, Fe, and Cr by electrodeposition techniques, (2) the incorporation of heavy metal ion impurities, such as Sr, Ce, Cr, Fe, and U, in aqueous solutions into hydrous nickel oxide films, used as a model system, and (3) characterization of the structure of the impurity ions and the host oxides "in-situ" by synchrotron X-ray absorption and laser Raman spectroscopies.

Corrosion processes are basically electrochemical in nature, and the deposition of corrosion products on surfaces can best be simulated by electrochemical techniques, e.g., via cathodic precipitation and anodic electrodeposition from solutions of the metal ion of interest. Thus, $Ni(OH)_2$ films were prepared by cathodic electrolysis of $Ni(NO_3)_2$ solution at constant current similar to that employed by Capehart et al. [2]; NiOOH films were formed by anodic deposition at positive potentials close to oxygen evolution from Ni(II) sulfate plus acetate solutions, as was done by Chen and Noufi [3]. Iron oxide films were similarly prepared by constant potential electrolysis from dilute solutions of Fe(II) in borate buffer solution [4], as well as by standard chemical procedures.

Incorporation of Sr, Ce, Cr, Fe, and U into the oxide films was carried out by co-precipitation during the electrodeposition process. Stable isotopes of Sr, Ce, Cr, and Fe were used to facilitate the measurements; U was studied in its state of natural abundance in the starting material of uranyl nitrate.

Synchrotron X-ray Absorption Spectroscopy (XAS), both X-ray Absorption Near Edge Structure (XANES) and Extended X-ray Absorption Fine Structure (EXAFS), was employed as the principal technique for obtaining structural information on the host oxide film and the local structure of the impurity ion [5]. This is because of the high degree of disorder of the surface films, which makes it difficult to obtain structural parameters by X-ray Diffraction (XRD). A special X-ray/electrochemical cell was fabricated for the purpose of carrying out simultaneous electrochemical and "in-situ" XAS studies [6]. The measurements were carried out at various beamlines in the NSLS, SSRL, and APS. Both transmission and fluorescence detection techniques were employed. Where possible, measurements were made as a function of temperature from 298 to 77 K. Measurements were carried out at the K-edges of Ni, Fe, and

Sr, while Ce and U were studied at their respective L(III)-edges. The corresponding edge energies are: 8.333, 7.112, 16.105, 5.105, and 17.166 keV, respectively. In some cases, Raman spectroscopic measurements were carried out to supplement the structural information obtained from XAS.

RESULTS

A summary of our major findings is presented here. Details of the results, experimental procedures, and discussions can be found in our publications, which are listed at the end of this report, or in the open literature.

Structure of Hydrous Nickel Oxide Films

We have chosen hydrous nickel oxides as model systems because of the variety of sites into which heavy metal ions can be incorporated, e.g., lattice vacancies, interlamellar sites, and surface defects; they can also be incorporated as outer or inner sphere complexes [7]. We have studied the incorporation of Sr, Ce, Cr, Fe, and U into electrodeposited $Ni(OH)_2$ and, in some cases, in NiOOH films. The host oxides were deposited on a graphite substrate. This substrate was chosen in order to facilitate examination of the oxide film without interference from an underlying base metal and also to allow XAS measurements to be carried out with both fluorescence and transmission detection techniques. $Ni(OH)_2$ was cathodically deposited from a 0.1 M $Ni(NO_3)_2$ solution at a current density of about 8 mA/cm^2 for 5 to 15 minutes [2]. The deposit was greenish in color and has been shown to be α-$Ni(OH)_2$ from XRD and XAS measurements [2,8]. The EXAFS data show the Ni to be coordinated to 6 oxygen first neighbors at 2.05 Å and to 6 nickel second neighbors at 3.10 Å. The electrochemically deposited α-$Ni(OH)_2$ appears more disordered than β-$Ni(OH)_2$, which we also prepared chemically.

NiOOH films were prepared by anodic deposition at a constant potential of 1.10 V vs. a saturated calomel electrode reference (SCE) from a solution of 0.05 M $NiSO_4$ + 0.5 M Na_2SO_4 for 0.5 to 10 hours. The films deposited have good adherence. XAS measurements show the

film to consist of a mixture of Ni^{2+} and Ni^{4+}. The film could be further oxidized in KOH solution in order to convert it nearly completely to Ni^{4+} material. Figure 1 shows the XANES spectrum of the electrodeposited material compared to those of a number of nickel compounds, which we have extensively studied and used as standard references [9,10]. The shift in K-edge energy to higher values is evident as one goes from Ni^0 to Ni^{2+} to Ni^{4+} (as in $KNiIO_6$). The ability of Ni to form Ni^{4+} is of great importance in the development of Ni-based batteries. The electrodeposited nickel oxide film-on-graphite has also been found to possess high charge storage capability and would be useful in the fabrication of ultracapacitors [6].

Figures 2a and 2b show the EXAFS function for electrodeposited NiOOH and the corresponding Fourier Transform (FT). Quantitative fitting yields two Ni-O bond distances at about 1.88 Å and 2.05 Å, and one Ni-Ni bond distance at 2.82 Å. From a comparison with standard Ni^{2+} and Ni^{4+} compounds [9,10], we associate the 1.88 Å and Ni-O distance to a Ni^{4+} species and the distance of 2.05 Å to a Ni^{2+} species in the film. The Ni^{2+} phase appears to be more disordered than the Ni^{4+} phase. The Ni-Ni bond distance of 2.82 Å is assigned to the Ni^{4+} species, since it is too short to be attributed to α-$Ni(OH)_2$ in the film.

INCORPORATION OF HEAVY METAL IONS

Local Structure of Strontium in Nickel Oxide Films

Figure 3a shows the $\chi(k)$ function for Sr^{2+} which was co-deposited cathodically with $Ni(OH)_2$ from a solution of 0.1 M $Ni(NO_3)_2$ + 0.01 M strontium acetate at a current density of 8 mA/cm^2 for 17 min. Also exhibited is that for Sr^{2+} in a 0.1 M strontium acetate solution. It is evident that the two are very similar. The corresponding FTs shown in Fig. 3b further indicate a close similarity in the structure of the Sr^{2+} ions in solution with those co-deposited in the oxide film. The FT shows only one prominent first near-neighbor peak consistent with oxygen atoms in the first shell. Peaks at further distances could not be discerned within the accuracy of the present measurement. This could be due to the relatively large disorder in the film**.** Fitting of the EXAFS data yields a Sr-O bond distance of 2.58 $\pm$ 0.02 Å. The α-$Ni(OH)_2$ lattice appears relatively unaffected, suggesting that the strontium oxide (hydroxide) phase

probably forms separate domains during the co-precipitation process. Intercalation or lattice substitution of Sr^{2+} was not detected in the experiments.

Sr^{2+} was also co-deposited with anodically formed Ni-oxide film from a solution of 0.05 M $NiSO_4$ + 0.5 M sodium acetate + 0.1 M strontium acetate at an applied potential of 1.1 V vs. SCE for about 8 hours. The XAS spectrum of Sr^{2+} was very similar to that in the cathodically deposited nickel oxide film. It is interesting to note that a pure Sr-containing film can be prepared by anodization at 1.2 V vs. SCE in a solution of 0.1 M strontium acetate for 1 hr and 20 min. The XAFS spectrum of the film showed a slight difference compared to that of a Sr-in-NiOOH film; distinct higher shell peaks present in the pure Sr film are absent in the co-deposited material. Structural parameters for the first peak of the FT were obtained by fitting the data to a Sr-O standard generated using the FEFF6 computer program [11]. In both samples, the Sr appears coordinated to about 8 to 10 oxygen neighbors. The Sr-O bond distances for the pure Sr and that co-deposited in the film with NiOOH were calculated as 2.595 Å and 2.625 Å, respectively. These are again similar to the Sr-O distance of 2.6 Å obtained for Sr^{2+} in aqueous solutions [12].

Incorporation of Cerium into Nickel Oxide Films

Cerium is representative of the lanthanide group of radionuclides. Its incorporation into oxide films is of interest not only from the standpoint of environmental remediation but also for other practical applications, e.g., in corrosion inhibition [13,14]. We have studied its incorporation into nickel oxide films by co-precipitation processes. In contrast to Sr, Ce can assume valency states of 2+ and 3+ over potential regions commonly encountered in aqueous solution environments. Figure 4 shows the cyclic voltammogram of a graphite electrode in a solution of 0.05 M $NiSO_4$ + 0.5 M sodium acetate + 0.04 M Ce(III) acetate. Waves A_2 and C_2 correspond to the anodic oxidation of Ni^{2+} and electroreduction of the corresponding product, respectively. Waves A_1 and C_1 are due to the oxidation/reduction reactions of Ce^{3+} in solution. It may therefore be anticipated that formation of Ni^{2+} films would incorporate Ce^{3+}, while at more oxidizing conditions where Ni^{3+} and Ni^{4+} are formed, the films should contain Ce^{4+}. XAS measurements did confirm the latter, but it was surprising to find that even at fairly cathodic

potentials, some Ce^{4+} appeared in the $Ni(OH)_2$ films. The general appearance of the near-edge spectra (XANES) of Ce is a good fingerprint of the valence state of Ce in its oxides/hydroxides. This is illustrated in Fig. 5 for the spectra of Ce(III) acetate and $Ce(OH)_4$. Ce^{3+} ions exhibit an intense single white line at the threshold energy, which is attributed to a resonance in the 2p to 5d atomic cross-section modified by local density of unoccupied states. Tetravalent Ce, on the other hand, shows a double peak structure at the absorption edge.

Figure 6c shows the XANES spectrum of Ce incorporated into a NiOOH film by anodic co-deposition at 1.1 V vs. SCE from a solution of 0.05 M $NiSO_4$ + 0.5 M sodium acetate + 0.04 M cerium(III) acetate. The double peak indicates the presence of Ce^{4+} in the film. Interestingly, we found it possible to anodically deposit a pure cerium oxide film by constant potential electrolysis at 1.1 V vs. SCE with a graphite electrode in 0.08 M Ce(III) acetate solution. The XANES spectrum (Fig. 6d) is quite similar for that of Ce in the NiOOH film. We also find subtle differences in the XANES of our standard $Ce(OH)_4$ and CeO_2 samples, as can be discerned from Figs. 6a and 6b. The CeO_2 standard clearly shows the peak "C" to be more intense than "D", as well as the prominence of the shoulders "A" and "B". The $Ce(OH)_4$ is structurally disordered, while the CeO_2 is more crystalline, as can be seen from the XRD pattern in Fig. 7. Moreover, the laser Raman spectrum of the $Ce(OH)_4$ material (Fig. 8a) does not show the sharp OH stretching band in the region of about 3600 cm^{-1} that is characteristic of true hydroxides. Instead we found a rather broad band that is more typical of the presence of water in the structure (Fig. 8b). It is likely that the material is really a form of CeO_2 with a highly disordered structure due to the presence of water. We will nevertheless refer to it as $Ce(OH)_4$. From plots of $k^3 \chi(k)$ and the corresponding FTs, it was evident that the state of Ce codeposited with the NiOOH film is closer to $Ce(OH)_4$ than CeO_2. Structural parameters were obtained by fitting the Ce EXAFS data to theoretical spectra calculated using the FEFF6 program. Derived parameters are shown in Table I.

Co-deposition of Ce with $Ni(OH)_2$ film was carried out in a solution of 0.04 M cerium(III) acetate + 0.1 M nickel acetate at constant current. The Ce in the film appeared to be mostly Ce^{3+} with a small amount of Ce^{4+}. The latter appeared to be always present in the aqueous solutions of Ce(III) acetate that we have examined.

Selective Site Occupancy of Chromium in Nickel Hydroxide Films

These investigations are also relevant to the general problem of remediation of chromium from the soil and groundwaters. The widespread use of chromium in industrial applications, such as tanning and plating, has led to its contamination of groundwaters. The most stable states of Cr in the environment are Cr^{3+} and Cr^{6+}. The latter is of great concern due to its toxic and carcinogenic properties. On the other hand, Cr^{3+} is relatively immobile and nontoxic. There has been a considerable effort to reduce Cr^{6+} to Cr^{3+} by forming insoluble Cr^{3+} precipitates [15,16,17].

The oxidation state of chromium incorporated into simulated corrosion films of nickel was investigated initially by using the XANES technique. The XANES spectra of Cr^{6+} compounds exhibit a prominent pre-edge feature that is attributed to the 1s to 3d transition. In contrast, the XANES of Cr^{3+} compounds exhibit only minor pre-edge peaks. Hence, the general appearance of the XANES is a good fingerprint for the oxidation state of chromium.

Figure 9 shows the XANES of chromium in K_2CrO_4 (Cr^{6+} standard) and Cr_2O_3 (Cr^{3+} standard) compared with those of Cr^{6+} and Cr^{3+} solutions. The difference in the XANES for the two valence states can be clearly seen. A prominent pre-edge peak is present in the case of Cr^{6+}, but only minor peaks are seen for Cr^{3+}.

Figure 10 shows a comparison of the "in situ" XANES of chromium in a pure chromium oxide film prepared by cathodic deposition from a solution containing Cr^{3+}, and in a mixed oxide film where chromium was cathodically co-deposited with nickel from a solution containing Ni^{2+} and Cr^{3+}. In both films, there are only minor pre-edge features, which indicate that chromium in these films is present in the 3+ oxidation state. However, the shape of the XANES for these two films is not the same, suggesting that the chromium-containing phase formed on co-deposition is different from the phase found in the pure chromium oxide film.

Figure 11 shows the result of XAS measurements on a sample of pure chromium oxide film prepared by cathodic deposition from a solution containing Cr^{6+}, and a sample of a mixed oxide film where chromium was cathodically co-deposited with nickel from a solution

containing Ni^{2+} and Cr^{6+}. Curve (b) shows the XANES obtained "in situ" on the pure chromium oxide film, taken within 10 min following deposition. It can be seen that the XANES exhibits a small but noticeable pre-edge peak. This indicates that most of the chromium in this sample exists in the 3+ oxidation state; however, a small amount of Cr^{6+} is also present. The presence of some chromium atoms in the 6+ state might be due to some sorbed Cr^{6+} ions that are on the surface or in the pores of the Cr^{3+} phase and are not in electrical contact with the electrode.

Curve (a) in Fig. 11 corresponds to the "in situ" chromium XANES in the mixed oxide sample. In contrast to the previous cases, we find that the XANES exhibits a prominent pre-edge peak, indicating that the chromium is present in the 6+ oxidation state. This is a very surprising result since one expects chromium to be present in the 3+ oxidation state on cathodic deposition. It indicates that cathodic co-deposition of Cr^{6+} and Ni^{2+} leads to a chromium oxide film in which chromium is present in the 6+ oxidation state. The phase does not reduce to a Cr^{3+} phase even on exposure to ambient air for several hours. This is in contrast to studies by Bardwell et al. [18] on passive Fe-Cr films, who found that the Cr^{6+} in the passive film was relatively unstable and was reduced on exposure to air.

Figure 12 shows the "ex-situ" Ni edge XANES in pure cathodically deposited $Ni(OH)_2$ film (a) and in the co-deposited films with Cr. It is evident that the edge positions of all samples concide within the uncertainty of 0.2 eV. Thus, Ni exists in the 2+ oxidation state in all the films studied.

We subsequently utilized EXAFS to more fully define the local structure of Cr^{3+} and Cr^{6+} ions incorporated into electrodeposited α-$Ni(OH)_2$ films. The incorporation of Cr^{3+} into α-$Ni(OH)_2$ was carried out by co-deposition from a solution containing 0.0005 M $Cr(NO_3)_3$ and 0.1 M $Ni(NO_3)_2$ for 30 minutes at a constant cathodic current of 5 mA/cm^2 (Sample I). The incorporation of Cr^{6+} was carried out by co-deposition from a deaerated solution of 0.001 M K_2CrO_4 and 0.1 M $Ni(NO_3)_2$ for 16 min at a constant cathodic current of 5.13 mA/cm^2 (Sample II).

Figure 13 shows the EXAFS $\chi(k)$ function of Cr absorbers in sample (I) and sample (II). The $\chi(k)$ spectra of the two samples are distinctly different, which clearly indicates that the local environment around Cr in the two samples is not the same. This analysis becomes more explicit when $\chi(k)$ is Fourier transformed. Figure 14 shows the k^3-weighted FT of Cr absorbers in the two samples. The general appearance of the FT of sample (I) is similar to that of Ni absorbers in α-$Ni(OH)_2$, which has been reported earlier in several studies [19]. This suggests that the local environment of Cr in sample (I) is similar to that of Ni in α-$Ni(OH)_2$. We note that the FT of sample (I) shows a peak centered at ~5.60 Å and is shown in the lower inset of Figure 14. This peak is also seen in the FT of Ni absorbers in nickel hydroxide. This peak arises due to scattering from Ni neighbor atoms at ~6.18 Å in nickel hydroxide; its intensity is enhanced due to the focusing effect of the intervening shell of Ni atoms at ~3.09 Å (within the brucite layers) [19]. The peak thus serves as a fingerprint which clearly indicates that Cr in sample (I) occupies Ni lattice sites. Non linear least square fits of the data in the r-range 1.05-3.40 Å show that Cr atoms in sample (I) are coordinated to 6.0(6) oxygen first near-neighbors at 1.99(1) Å and to 5.8(7) Ni atoms at 3.09(1) Å. The Cr-O bond distance of 1.99 Å is similar to those found in Cr^{3+} compounds such as $Cr(OH)_3$ and Cr_2O_3 [20]. This indicates that Cr in sample (I) is present in the 3+ oxidation state. Representing the second shell as a Cr-Cr correlation instead of a Cr-Ni correlation resulted in fits that were ~40% worse in quality, indicating that Cr is surrounded predominantly by Ni in the second shell. The Cr-Ni distance of 3.09 Å is identical to the Ni-Ni distance found in α-$Ni(OH)_2$ and is further evidence of Cr occupying Ni lattice sites in α-$Ni(OH)_2$ [19].

The FT of Cr absorbers in sample (II) is distinctly different from that of Ni in nickel hydroxide. This suggests that Cr does not enter the Ni lattice site in this system. Detailed fitting shows that the first major peak in the FT can be well represented by ~3.8(5) oxygen atoms at 1.66(1) Å. This suggests that Cr is surrounded by oxygen atoms located in a symmetric tetrahedra, as in CrO_4^{2-} [21]. The Cr-O bond distance is consistent with what is expected for a Cr^{6+} compound [20,21]. The presence of Cr^{6+} is surprising as these films were prepared by cathodic co-deposition. In addition to the Cr-O peak, the FT of Cr absorbers in sample (II) also shows a small but clear peak centered at ~3.10 Å and is illustrated in the upper inset of Fig. 14. This peak shows the presence of higher shell neighbors as well. Quantitative

fitting of the data in the r-range 0.95-3.70 Å shows that, in addition to the 4 oxygen atoms at 1.66 Å, 1.9(8) Ni atoms at 3.41(5) Å are also present. The large uncertainty in the structural parameters of the Ni shell is due to the relatively weak contribution from this shell of atoms. As the peak at ~3.10 Å is relatively weak we find that this interaction can also be represented as a Cr-Cr correlation at 3.44(5) Å instead of a Cr-Ni correlation. A Cr-Ni/Cr distance of 3.41-3.44 Å is too large when compared to the Ni-Ni interaction found in α-$Ni(OH)_2$ (3.09 Å) or the Cr-Cr interaction found in Cr^{6+} compounds such as $K_2Cr_2O_7$ or CrO_3 (3.15-3.31 Å) [22]. This shows that the Cr^{6+} ions neither enter Ni lattice sites of α-$Ni(OH)_2$ nor form surface precipitates of pure or mixed hydroxides. Our findings are more consistent with Cr being present as a chromate group in the interlamellar spacings. Based on a Ni-O distance of 2.05 Å in α-$Ni(OH)_2$ and the experimentally determined Cr-O and Cr-Ni distances in sample (II), we infer that the chromate group is bonded to α-$Ni(OH)_2$ with a Cr-O-Ni bond angle of ~ 133°. This bond angle also suggests that the chromate group is bonded in a monodentate fashion, thus sharing a single oxygen with the Ni-O octahedra of the α-$Ni(OH)_2$ lattice. The presence of a symmetric oxygen shell around Cr and a Cr-O-Ni bond angle of 133° excludes the possibility of bidentate or tridentate bonding, as such configurations will lead to a significantly shorter Cr-Ni distance than observed.

In summary, our XANES and EXAFS measurements indicate that cathodic deposition from a 0.01 M $Cr(NO_3)_3$ solution at constant current results in a Cr^{3+} oxide (hydroxide) film. Deposition from a 0.01 M K_2CrO_4 solution produces a film which is predominantly Cr^{3+} but with some Cr^{6+}. This material is air-sensitive, and the ratio of Cr^{6+} to Cr^{3+} increases with time of exposure to ambient. Cathodic co-deposition of Cr^{3+} and Ni^{2+} leads to the incorporation of Cr^{3+} in Ni lattice sites of α-$Ni(OH)_2$. In the cathodic co-deposited film of Cr^{6+} and Ni^{2+}, Cr surprisingly exists as Cr^{6+} and occupies the interlamellar regions as a chromate group coordinated to the brucite layers of α-$Ni(OH)_2$ in a monodentate fashion.

Local Atomic and Electronic Structure of Iron

In view of its importance as a basic metal and as a major component in alloys like steel, we have carried out more extensive studies on this material. We investigated the local atomic

and electronic structure of iron incorporated into electrodeposited nickel hydroxide films. Briefly, we found that cathodic codeposition from a solution of Fe(II) and nickel nitrate results in iron occupying Ni lattice sites in α-$Ni(OH)_2$, but as Fe(III)! EXAFS showed that Fe is coordinated to oxygen at ~2.00 Å and to Ni at ~3.11 Å. This Fe-O bond length is smaller than the Fe(II)-O bond distance found in $Fe(OH)_2$ (~2.10 Å) but is in good agreement with the average Fe(III)-O bond distance found in FeOOH (α,γ). The Fe-Ni bond distance is in agreement with that of the Ni(II)-Ni(II) bond distance found in α-$Ni(OH)_2$. Moreover, the radial structure function (RSF) around Fe showed a distinct peak at ~5.8 Å, which is a fingerprint of the brucite α-$Ni(OH)_2$ structure. On anodic oxidation of the codeposited film in KOH, we found that the Fe ions occupied Ni lattice sites in γ-NiOOH. The XANES showed that the Fe edge shifted to higher energies, indicating an increase in the oxidation state of Fe on charging. The EXAFS indicated that Fe is coordinated to oxygen at ~1.94 Å and to Ni at ~2.84 Å. The latter value is in good agreement with the Ni(IV)-Ni(IV) bond length found in γ-NiOOH. The RSF around Fe in the oxidized film showed a distinct peak at ~5.4 Å, just as in the RSF of Ni in γ-NiOOH. The Fe-O bond distance of ~1.94 Å is in good agreement with the Fe(IV)-O bond distance found in $SrFeO_3$. Our results suggest that the Fe ions in the oxidized film are nominally tetravalent but that the Fe-O bond possesses a high degree of covalency.

There has been a number of studies designed to understand the local atomic and electronic structure of iron and other metal ions incorporated into α-$Ni(OH)_2$ [23-29]. For brevity, we omit discussion of previous works here. The reader is also referred to our papers for details of our experimentation, results, and data analysis (cf. paper number 9).

The Ni EXAFS and RSF of the Fe-doped hydrous nickel oxide films are similar to those of the corresponding pure hydrous nickel oxide films. To within the sensitivity of the EXAFS technique, the local structure of Ni remains the same in both α-$Ni(OH)_2$ and γ-NiOOH upon incorporation of Fe. This is similar to results from the Ni EXAFS in other co-deposited systems [28,29,30].

A systematic linear shift in the Fe edge position as a function of the oxidation state of Fe [Fe(0) to Fe(III)] has been reported [31]. Conceptually, this can be understood as due to an

increase in the attractive potential of the nucleus on the 1s core electron as the formal valence increases. Figure 15 shows a comparison of the Fe XANES of the various samples with the reference standards Fe(0) and α-FeOOH [Fe(III)]. The threshold energy E_0 is defined at the first inflection point of the absorption edge of Fe foil. It can be seen that the edge position of Fe in α-$Ni(OH)_2$ is almost coincident with that in α-FeOOH; that of Fe in the chemically prepared pure hydrous iron oxide sample occurs at a much lower energy value. This shows that, in the pure hydrous iron oxide sample, iron is present as Fe(II), i.e., most likely as $Fe(OH)_2$. However, on cathodic co-deposition from a solution containing Fe(II) and Ni(II), Fe was found to be present as Fe(III) in the deposited material. It is surprising to find Fe in an oxidized state upon cathodic codeposition. As noted earlier, a similar oxidation of Co(II) to Co(III) on cathodic codeposition with α-$Ni(OH)_2$ has been reported by others [29,30]. It appears that α-$Ni(OH)_2$ provides a suitable matrix for the oxidation of these ions.

Figure 15 also illustrates the change in oxidation state of Fe resulting from the electrochemical oxidation of the Fe doped α-$Ni(OH)_2$ film in KOH. It can be seen that the overall shape of the Fe XANES changes distinctly on oxidation; this suggests a change in the local environment of Fe. Further, on oxidation the edge position shifts to higher energies. This shows that the average oxidation state of Fe increases on charging. This is in sharp contrast to the findings of Kim et al. [29] who reported that the oxidation state of Fe ions in hydrous nickel oxides prepared electrochemically from a solution containing Fe(III) and Ni(II) does not change on oxidation and always remains as Fe(III).

As shown in Fig. 15, the shift in edge position between Fe(III) in α-$Ni(OH)_2$ and the oxidized film is smaller than the shift from Fe(II) to Fe(III) [between the pure hydrous iron oxide sample and Fe(III) in α-$Ni(OH)_2$]. An edge shift of magnitude similar to those seen in our Fe-doped films was reported by Choy et al. [32] in a recent EXAFS study of the electrochemical oxidation of $SrFeO_{2.5}$ (brownmillerite) to $SrFeO_3$ (perovskite). They interpreted the edge shift to represent a change in oxidation state of Fe from Fe(III) to Fe(IV). $SrFeO_3$ is a cubic perovskite in which Fe is nominally tetravalent. There have been a number of studies to understand the local electronic structure of $SrFeO_3$ and other related oxides. On the basis of photoemission spectroscopy, Bocquet et al. [33] suggested that the ground state of

Fe is not d^4 [as expected for ionic Fe(IV)] but rather heavily mixed d^4 and $d^5\underline{L}$ states (where $\underline{L}$ indicates an oxygen 2p hole). This suggests that the Fe-O bond in $SrFeO_3$ has a high degree of covalency. Consequently, one expects that the charge transfer from the ligand will greatly reduce the formal charge on the Fe atom, thereby reducing the edge shift seen in the XANES spectra. The presence of a high degree of covalency in the Fe-O bond of $SrFeO_3$ has been experimentally verified by Abbate et al. using soft x-ray spectroscopy [34]. They found that the Fe 2p x-ray absorption spectra do not show the $2p^63d^4 \rightarrow 2p^53d^5$ multiplet structure expected for the d^4 ionic ground state. Based on this information we suggest that the oxidation state of Fe in the Fe-doped NiOOH film is similar to that of Fe in $SrFeO_3$, i.e., Fe is nominally tetravalent. However, due to the large covalency of the Fe(IV)-O bond the XANES edge shift is smaller than anticipated. Reduced edge shift due to higher covalency of the metal-ligand bonds has been observed in several other cases [35,36]. The concept of coordination charge, where the formal charge of a metal is reduced by a factor corresponding to the degree of covalency of the bonding ligand, has been employed to explain differences in absorption edge shifts [35,36]. Further evidence for the increase in the oxidation state of Fe in the codeposited film on anodic oxidation in KOH can be obtained by analyzing the EXAFS spectra.

Figure 16 shows the EXAFS spectra and RSF of Fe absorbers in the chemically prepared pure hydrous iron oxide sample. It can be seen that qualitatively the RSF of Fe is similar to the RSF of Ni absorbers in α-$Ni(OH)_2$ (Fig. 17). In particular, we note that the RSF in Fig. 16b exhibits a peak around ~6 Å (enlarged in the inset). The presence of this peak indicates that the pure hydrous iron oxide sample takes on a brucite-like structure, expected for $Fe(OH)_2$ [22]. Quantitative analysis of the Fe EXAFS was performed by fitting the first two peaks of the RSF. We find that these two peaks can be well represented as an Fe-O correlation at ~2.10 Å and an Fe-Fe correlation at ~3.20 Å. The structural parameters obtained on fitting are given in Table II. The Fe-Fe bond distance of 3.20 Å is larger than the Co-Co (3.17 Å) or the Ni-Ni (3.13 Å) bond distance found in β-$Co(OH)_2$ and β-$Ni(OH)_2$, respectively; this indicates a gradual decrease in the metal-metal bond distance with increasing atomic number of the transition metal atom [28,30,37,38].

Figure 18a shows a comparison of the EXAFS $\chi(k)$ functions of Fe absorbers incorporated into the α-$Ni(OH)_2$ and γ-NiOOH films. In both "in situ" and "ex situ" measurements, the oscillations are in phase for the Fe-doped α-$Ni(OH)_2$ samples. This indicates that the local atomic structure of Fe in α-$Ni(OH)_2$ does not change significantly even on extended exposure to ambient. However, the amplitude of the $\chi(k)$ function in the "ex situ" measurements appears to be larger in the high-k region. This suggests a higher degree of order for the film exposed to ambient. In contrast, the $\chi(k)$ function of Fe in γ-NiOOH is distinctly different from that of Fe in α-$Ni(OH)_2$. This suggests that the local structure of Fe is modified upon oxidation. These qualitative comparisons become explicit on Fourier transformation as illustrated in Fig. 18b. It can be seen that the major peaks in the RSF of Fe absorbers in Fe-doped α-$Ni(OH)_2$ occur at roughly the same r values for both the "in situ" and "ex situ" measurements. However, the amplitudes of the peaks in the "in situ" measurement are smaller than those in the "ex situ" measurement. Also, the general appearance of the RSF of Fe absorbers in Fe-doped α-$Ni(OH)_2$ is similar to the RSF of Ni in α-$Ni(OH)_2$ (Fig. 17). In particular, as in α-$Ni(OH)_2$, the RSFs of Fe absorbers in Fe-doped α-$Ni(OH)_2$ show a peak around 5.8 Å (enlarged in the inset of Fig. 18b) in both the "in situ" and "ex situ" measurements. This peak, though small, is significantly above background. Further, the overall shape and position of the peak do not change significantly on changing the k-limits of the Fourier transform. This suggests that the peak represents a real correlation. The presence of this peak reveals that the Fe ions occupy sites in a brucite-like structure, similar to those of Ni ions in α-$Ni(OH)_2$.

Quantitative analysis of the Fe EXAFS in the Fe-doped α-$Ni(OH)_2$ sample was performed by fitting the first two peaks in the RSFs. The structural parameters obtained on fitting are given in Table II. Comparisons of the fits obtained to experimental data are given in Figs. 19a and 19b. We find that in both "in situ" and "ex situ" measurements the first two peaks can be well represented as an Fe-O correlation at ~2.00 Å and an Fe-Ni correlation at ~3.11 Å. The Fe-O bond distance is smaller than the Ni(II)-O bond distance (~2.05 Å) found in α-$Ni(OH)_2$. The Fe-Ni bond distance is comparable to the Ni-Ni bond distance (~3.09 Å) found in α-$Ni(OH)_2$. Due to the proximity of Fe and Ni in the periodic table these two

backscatterers cannot be easily distinguished by EXAFS spectroscopy. Therefore, the second peak in the RSF of Fe-doped α-$Ni(OH)_2$ can also be represented as an Fe-Fe correlation. Representing the second shell as an Fe-Fe correlation rather than an Fe-Ni correlation results in an Fe-Fe bond distance of 3.14 Å. It is now important to verify that a separate hydrous iron oxide phase is not formed on codeposition. From the XANES measurements we know that in Fe-doped α-$Ni(OH)_2$, Fe exists as Fe(III). This rules out the presence of Fe as $Fe(OH)_2$. Moreover, the Fe-O bond length of ~2.00 Å in the codeposited film is smaller than the Fe(II)-O bond (~2.10 Å) found in the pure Fe(II) hydrous oxide sample. However, the average Fe(III)-O bond distance in FeOOH polymorphs (α, γ) is ~2.00 Å [39-42]. Neutron diffraction measurements indicate that in α-FeOOH the first oxygen shell is split into two sub-shells at 1.95 Å and 2.09 Å, giving an average Fe(III)-O distance of ~2.02 Å [41]. These distances are in good agreement with EXAFS measurements on α-FeOOH [40]. In γ-FeOOH, EXAFS measurements indicate that the first shell consists of 6 oxygen atoms at ~1.99 Å [40]. This Fe-O distance is in good agreement with X-ray diffraction measurements on γ-FeOOH [42]. Therefore, an Fe-O bond distance of ~2.00 Å found in the cathodically codeposited films is consistent with what is expected for an Fe(III) ion in a hydroxide. However, the absence of a pure Fe(III) hydroxide phase can be ascertained by examining the higher shell correlations. In β-and α-FeOOH the second coordination shell contains two well-resolved Fe-Fe correlations due to the presence of corner-sharing linkages in addition to edge sharing [39,40,43]. In γ-FeOOH the Fe-Fe correlation from edge sharing linkage occurs at ~3.06 Å, which is smaller than the Fe-Fe correlation (~3.14 Å) seen in the co-deposited films [40,42,43]. From the above discussions we see that the presence of Fe as FeOOH (α, β, γ) in the cathodically codeposited film can be ruled out. Thus, based on the local structural parameters and the presence of a peak at ~5.8 Å in the RSF of Fe-doped α-$Ni(OH)_2$, we conclude that Fe atoms occupy Ni lattice sites in α-$Ni(OH)_2$.

Figure 18b also shows the RSF of Fe in the oxidized film. It can be seen that on oxidation the Fe-O shell shifts slightly to lower r values while the Fe-Ni shell shifts significantly (when compared to the Fe-doped α-$Ni(OH)_2$]. Also, the general appearance of the RSF of Fe in the oxidized sample is similar to that of Ni in γ-NiOOH. In particular, just as

in γ-NiOOH (Fig. 17), the RSF of Fe absorbers in the oxidized sample shows a prominent peak around ~5.4 Å. This suggests that Fe ions also occupy Ni lattice sites in γ-NiOOH upon oxidation of $Ni(OH)_2$. Quantitative analysis of the data was performed by fitting the first two peaks in the RSF. The structural parameters obtained on fitting are given in Table II, and a comparison of the fit to experimental data is illustrated in Fig. 19c. We find that the first two peaks of the RSF can be well represented by an Fe-O correlation at ~1.94 Å and by an Fe-Ni correlation at ~2.84 Å. The Fe-O bond distance is larger than the Ni(IV)-O correlation (~1.88 Å) found in γ-NiOOH. The Fe-Ni bond distance is comparable to the Ni(IV)-Ni(IV) bond distance (~2.82 Å) found in the γ-NiOOH. This Fe-Ni bond distance of ~2.84 Å is further evidence for Fe occupying sites surrounded by Ni(IV) ions of the γ-NiOOH structure. The Fe-O bond distance of ~1.94 Å found in the oxidized sample is smaller than the Fe(III)-O bond distance (~2.00 Å) found in the Fe-doped α-$Ni(OH)_2$ films. This reduction in the Fe-O bond distance is in agreement with the XANES data, which indicate that the oxidation state of Fe increases on charging. Based on diffraction data the Fe(IV)-O bond distance in $SrFeO_3$ is ~1.93 Å [32,33]. The Fe-O bond distance in the oxidized sample is thus comparable to the Fe(IV)-O bond distance in $SrFeO_3$. We therefore conclude that on charging the Fe-doped α-$Ni(OH)_2$ film in KOH, Fe atoms occupy Ni lattice sites in γ-NiOOH and exist nominally in the Fe(IV) oxidation state, analogous to that of Fe in $SrFeO_3$.

We have also studied the anodic deposition of iron oxide thin films as carried out in a manner similar to that employed by Markovac and Cohen [4] using dilute solutions of Fe^{2+} in borate buffer solution. Again, for purposes of carrying out XAS measurements, a graphite substrate was used. The quantitative identification of the iron oxide films formed by the anodic deposition process has not been carried out previously and was an important objective of our studies. The composition and structure of the corrosion films on iron are still a subject of much debate even after over a hundred years [44].

Figure 20 shows a cyclic voltammogram of a graphite electrode in a deaerated solution of 0.005 M $FeSO_4$ + 0.3 M H_3BO_3 + 0.075 M $Na_2B_4O_7$ borate buffer solution. Deposition was carried out by holding the potential at 0.6 V vs. SCE for 490 min, over which time 0.155 coulomb/cm^2 of electric charge was passed. The XANES spectrum of the film formed taken

"in-situ" is shown in Fig. 21a. The film was subsequently reduced at -1.05 V and gave the spectra shown in Fig. 21b. The spectrum of an iron foil is shown in Fig. 21c for comparison. It is evident that reduction of the oxide film resulted in the formation of metallic iron with some unconverted (~30%) oxide still present. EXAFS spectra are shown in Fig. 22 and the corresponding FTs in Fig. 23. Comparison of the FT of the anodically deposited film with those of standard samples of Fe_3O_4, Fe_2O_3, and FeOOH suggests that the film consists mainly of γ-FeOOH. We find it most interesting that Kerkar et al. [45], using thin films of iron, also found by XAS that the corrosion film on iron is γ-FeOOH. This lends credence to the validity of our approach in simulating the formation of corrosion films on metals via electrodeposition processes.

Uranium Incorporation into Nickel Hydroxide Films

XAS studies of radioactive materials required the fabrication of a special spectro-electrochemical cell that incorporates additional safety features to ensure the proper containment of the sample. A double-containment cell that allowed for both transmission and fluorescence measurements was designed and fabricated to meet the stringent requirements at the Advanced Photon Source (APS), where these experiments were carried out.

Figure 24 shows the XANES at the U-L_3 edge of two deposited thin films compared with those for U(VI) and U(IV) solutions. The U(IV) solution was obtained by reducing a uranyl-nitrate solution with sodium formaldehyde sulfoxylate (commonly known as rongalite). The spectra of U(IV) shown in Fig. 24 were taken at the Advanced Photon Source (APS), beamline 12 BM-B (BESSRC-CAT). U(IV) was absorbed onto a piece of cloth, and few layers were stacked together. The U(VI) solution spectra were taken at the APS, beamline 10 ID-B (MR-CAT). The spectra were taken in the cell "in situ" prior to cathodic deposition. The two deposited films were measured "in situ" at beamline 10 ID-B. The energy calibration of all the spectra was performed by simultaneously measuring a reference standard. It can been seen from Fig. 24 that the edge positions of the U(IV) and U(VI) solutions are well separated, and the general shapes of the XANES are distinctly different. Specifically, we note that the U(VI) solution shows a distinct feature just above the edge (indicated by the arrow in Fig. 24). This

feature has been seen in numerous U(VI) oxides/hydroxides and is thought to arise from multiple scattering contributions involving the axial oxygens (O-U-O) in the UO_2^{2+} moiety [46,47,48]. Thus, in addition to the usual edge position, the presence of this feature is a fingerprint for the presence of U(VI) as oxide/hydroxide. As shown in Fig. 24, the edge positions for both films are closer to that of U(VI) in solution. Also, in both cases the multiple scattering feature involving the axial oxygens is clearly seen. These observations suggest that in both films the U is present predominantly as U(VI). Closer inspection shows that the edge position of U in the codeposited film, U + $Ni(OH)_2$, is almost coincident with that of U(VI) solution, while that of the pure U film is slightly shifted to lower values. This suggests that the pure U film might contain a small amount (<25%) of U(IV) contribution as well.

Figure 25 shows a comparison of the EXAFS $\chi(k)$ for the deposited films with that of U(VI) solution. It can be seen that the data have good S/N ratio out to ~ 14 $Å^{-1}$, and that the EXAFS spectra of the codeposited films, (U+Ni), measured either "ex situ" or "in situ", are identical. However, the EXAFS spectrum of the U(VI) solution is distinctly different. The U(VI) solution exhibits a distinctly different beat pattern around ~7.5 $Å^{-1}$, and also the EXAFS is not in phase in the high k region when compared to the codeposited films. The pure U(VI) film shows some similarity to the co-deposited films but is not exactly identical. Table III summarizes the structural parameters derived by analysis of the EXAFS data.

The qualitative comparisons in the previous paragraph become explicit on Fourier transformation of $\chi(k)$, as can be seen in Fig. 26. The FT of all the samples shows a large first peak around 1.2-1.7 Å; this peak is due to axial oxygen atoms surrounding U in the uranyl moiety. It can be seen that this peak maximizes at higher r values in the deposited films when compared to that of the U(VI) solution. This suggests that the U – O axial bond distance is larger in the deposited films. The equatorial shell of the oxygen atoms contributes to the second peak of the FT around 1.7-2.5 Å. This peak appears as a large single peak in the FT of U(VI) solution (the slight asymmetry of the peak is due largely to some overlap with the first peak). In the case of the deposited films this peak is no longer a single strong peak but splits into two distinct sub-shells. This suggests that the structure of the oxygen atoms in the equatorial plane of the uranyl moiety is different in the deposited films.

The contribution to the FT in the region 1.1-2.7 Å was fitted in r space by use of FEFFIT to phase and amplitude functions generated with FEFF 6. The S_0^2 was fixed at 0.91, the value found by fitting the U(VI) solution spectra. All data were transformed in the k range of 2.5-14 Å and fitted in the r range of 1.15-2.55 Å. The number of independent data points in the data set was 10 [given by (2□k □r)/□]. The maximum number of free parameters that was varied in the fits was 9 which is within the limits of the information content of the data sets. The U(VI) solution data could be modeled using two shells, one representing the axial oxygen shell and another representing the equatorial shell. We find 2 U-O_{axial} bonds at ~ 1.78 Å and 6 ± 1 U-O_{equ} bonds at ~ 2.42 Å. Attempts to represent the equatorial shell of atoms as two shells did not give improved fits. Two nearby shells can be resolved in the EXAFS spectra if the separation between the shells is greater than □/2 k. From Fig. 25 we can see that the upper limit of the EXAFS spectra is about ~14 $Å^{-1}$. Thus, the equatorial shell of atoms surrounding U(VI) in solution have bond distances within ~0.12 Å and appear as a single shell with large disorder.

In the case of the codeposited films, U+$Ni(OH)_2$, we found that the data can be modeled using three shells: one representing the axial oxygens and the other two representing the equatorial shell of atoms. We found ~ 2 U-O_{axial} at ~1.82 Å. The equatorial shell is split into two subshells: ~2.5 U-O_{equ1} at ~ 2.30 Å and ~ 2.5 U-O_{equ2} at ~ 2.47 Å. Note that this splitting of the equatorial shell is absent in the U(VI) solution. As the splitting is ~ 0.17 Å it can be easily resolved in the EXAFS data. Such a splitting is not present in uranyl carbonates or nitrates but is present in U(VI) hydroxides (precipitated chemically from uranyl nitrate solution) [49]. The total coordination number of the equatorial shell (~5) appears to be slightly larger than that for the chemically precipitated hydroxides (~4). Also, note that the U-O_{axial} distance in the electrodeposited films is ~ 0.04 Å larger than the U-O_{axial} distance in the U(VI) solution. Studies by Allen et al. [48] on chemically precipitated uranyl hydroxides have shown that the axial bond length increases with pH. Therefore, the larger bond distance in the electrodeposited films is probably due to an increase of pH near the electrode surface due to the reduction of nitrate ions during cathodic deposition.

In the case of the pure U film we again found that the FT in the region 1.15-2.55 Å can be well modeled by a three shell fit. We found that the U atom is surrounded by ~1.5 oxygen atoms at ~ 1.84 Å, ~4 oxygen atoms at ~ 2.28 Å, and ~ 2.4 oxygen atoms at ~ 2.47 Å. Note that at ~1.84 Å we find only 1.5 oxygen atoms. Fixing the coordination number of this shell at 2 (as expected for the uranyl moiety) results in fits that are worse in quality by a factor of three. Also, note that at ~2.28 Å we find ~4 oxygen atoms. This is larger than what we see in the codeposited samples. As mentioned earlier, the XANES spectra suggest the possible presence of some U(IV). The U(IV)-O bond distance in UO_2 is ~ 2.32 Å [51]. Note that this bond distance is similar to the U-O_{equ1} bond distance associated with the uranyl moiety. As the EXAFS data are bandwidth limited, it is not possible to include this bond distance in the fits. However, the presence of U(IV) will reduce the ratio of U(VI) to total U in the sample. EXAFS data represent a weighted average of the local environment of all the uranium atoms. Therefore, a reduction in the effective coordination number associated with the uranyl entity can be expected. In conjunction with the XANES results we suggest that ~ 25% of the sample might be present as U(IV). This will account for the decrease in the coordination number of the U-O bond at ~1.84 Å.

The FTs of the samples exhibit additional peaks. Single scattering paths involving low Z atoms do not contribute significantly to the FT beyond ~ 3 Å. However, in the presence of a focusing atom, multiple scattering paths involving low Z atoms might contribute significantly. The peak labeled A in Fig. 26 is seen in the deposited films as well as in the solution species. This peak probably arises due to multiple scattering involving the axial oxygens or multiple scattering involving focused U-O-N/C paths, which may be present in the samples. A similar peak has been reported by others in many U(VI) samples[46,50]. The peak has been attributed to multiple scattering. It is thus reasonable to assign this peak to MS contributions.

As additional observation, we note that peak B is present only in the deposited films (absent in the solution spectra). The peak occurs at approximately the same location in the codeposited samples ("in situ" and "ex situ") but at a lower r value than in the pure U film. This peak is probably due to a U-U correlation. Fitting the peak assuming U backscattering gives satisfactory results. We found the U-U bond distance to be ~3.87 ± 0.05 Å and 3.68 ±

0.06 Å in the codeposited and pure films, respectively. These distances correspond well with what is expected for uranium hydroxide. This suggests the presence of uranium in some form of hydroxide phase in these samples. In the codeposited films we could not detect any peaks that can be uniquely attributed to Ni, suggesting the absence of any direct U-Ni interaction in the system.

RELEVANCE

The application of the results obtained in this project to field problems was constantly kept in mind. It was facilitated by contacts with prospective users and attendance at conferences on decontamination and disposal problems. From the knowledge gained in this work, certain principles that would be useful in designing decontamination procedures are immediately apparent. Thus, it is evident that incorporation by lattice substitution into vacancies and in interlamellar positions is not likely to be common, especially for large metal ions, e.g. Sr^{2+}, U^{6+} ,etc. More facile and selective decontamination procedures such as acid washing and selective solvent dissolution by complexation could therefore be developed. Smaller metal ions which fit easily into vacancies in the defective structure of the host oxide or intercalate in the interlamellar structure would be more difficult to remove and thus require more drastic procedures. These ions may require hot acid washing, electropolishing, etc, to remove the whole surface coating. The use of electrochemical methods for radioactive decontamination is particularly interesting [51]. Electropolishing has been demonstrated [1] and appears promising; there is, however, a need for a better scientific understanding of the techniques that people have employed. Future work should address this issue. The novel concept of an "electrochemical brush" and other avenues for future work are discussed under the headings of "Productivity" and "Patents."

Finally, it is worthwhile to mention the relevance of the results obtained in this project to other areas of energy technology. Knowledge of the structure of metal ions incorporated into hydrous nickel oxides is of great importance in the further development of advanced nickel-based batteries, ultracapacitors, and electrochromic devices. Similarly, an understanding of the

structure of iron and chromium oxides/hydroxides is vital to the development of corrosion inhibitors and the general problem of corrosion prevention.

PRODUCTIVITY

This project accomplished the principal goal of obtaining fundamental knowledge on the nature of heavy metal and radioactive metal ion contaminants in hydrous oxide films.
The principles have been demonstrated in the case of hydrous nickel oxide films. Lack of time and manpower limited us from extending the studies to alloys of the base metals, i.e., stainless and carbon steels, as well as nickel alloys (Incalloy). Studies at temperatures above ambient (to about 95°C) would have also been highly desirable and fruitful. A more detailed investigation on the correlation between the nature of defects in the oxide films and the degree of incorporation of certain ions would be worthwhile for future work. These could be the basis for a longer term Basic Environmental Science Program that DOE could pursue. Application of the principles developed herein to the engineering and testing of decontamination procedures for actual field samples is a big area of further work that needs to be done.

PERSONNEL SUPPORTED

This project was instrumental in providing research support to Prof. Susan Mini, who is a faculty member in the Physics Department of Northern Illinois University (DeKalb, IL). Support was also provided for the further postdoctoral training of Dr. Mahalingam Balasubramanian in the areas of electrochemistry, materials science, and corrosion. New insights into environmental problems and techniques for their investigation were gained by Dr. Azzam Mansour of the Naval Surface Warfare Center.

PUBLICATIONS

1). X-ray Absorption Spectroscopy Studies of Electrochemically Deposited Thin Oxide Films- M. Balasubramanian, C.A.Melendres, A.N. Mansour, and S. Mini, in Mater. Res. Symp. Proc. **524**, (1998).

2). X-ray Absorption Spectroscopy Study of the Local Structure of Heavy Metal Ions Incorporated into Electrodeposited Nickel Oxide Films- M. Balasubramanian, C.A.Melendres, and A.N. Mansour, in J. Electrochem. Soc. **146**, 607 (1999).

3). Selective Site Occupancy Exhibited by Cr^{3+} and Cr^{6+} Incorporated into Electrochemically Deposited Nickel Hydroxide Films- M. Balasubramanian and C.A.Melendres, in Electrochem. and Solid State Lett. **2**, 167 (1999).

4). Integrated X-ray L Absorption Spectra: Counting Holes in Ni Complexes- H. Wang, P. Ge, C.G. Riordan, S. Brooker, C. G. Woomer, T. Collins, C. A. Melendres, O. Graudejus, N. Bartlett, and S. P. Cramer, in J. Phys. Chem. B **102**, 8343 (1998).

5). An X-ray Absorption Near-Edge Spectroscopy Study of the Oxidation State of Chromium in Electrodeposited Oxide Films- M. Balasubramanian and C.A. Melendres, Electrochim. Acta **44**, 2941 (1999).

6). Local Structure of Chromium Incorporated into Electrodeposited Nickel Hydroxide Films- M. Balasubramanian and C.A. Melendres, J. Synchrotron Radiat. **6**, 594 (1999).

7). An X-ray Absorption Study of the Local Structure of Cerium in Electrochemically Deposited Thin Films- M. Balsubramanian, C.A. Melendres, and A.N. Mansour, Thin Solid Films **347**, 178 (1999).

8). L-Edge X-ray Absorption Spectroscopy of Some Ni Oxycompounds: Ni Oxidation States- H. Wang, C.A.Melendres, F.M.F. de Groot, M. Balasubramanian, S. P. Cramer, submitted for publication in the J. Phys. Chem.

9). X-ray Absorption Fine Structure Study of the Incorporation of Iron into Electrodeposited Nickel Hydroxide Films- M. Balasubramanian and C.A. Melendres, submitted for publication in the J. Phys. Chem.

10). The Local Structure of Uranium in Co-deposited Nickel Hydroxide Films- M. Balasubramanian and C.A. Melendres, in preparation.

INTERACTIONS

The Principal Investigator and/or his representative participated in a number of meetings and conferences during the course of this project. Among these are:

1). Workshop on Molecular Environmental Science in the Soft X-ray Region, Lawrence Berkeley Laboratory, Berkeley, CA, March 27-28, 1997.
2). Environmental Management Science Program Workshop, Chicago, IL, July 27-30, 1998.
3). Workshop on Decontamination and Decommissioning Research, Savannah River Site, Aiken, SC, November 17-18, 1998.
4). Annual Review Meeting of the Characterization, Monitoring, and Sensor Technology-Crosscutting Program (CMST-CP), Gaithersburg, MD, March 10-11, 1999.
5). Annual Meeting of the American Ceramic Society, Indianapolis, IN, April 25-28, 1999.

PATENTS

No patent application was filed in this program. However, certain novel ideas for decontamination and disposal have been conceived in the course of this project. Among these are: 1) the development and use of an electrochemical brush, and 2) storage of radionuclides, such as uranium, in calcite, a highly defective oxide, and in clays. The embodiment of the first would be an electrically powered wire brush to which a voltage would be applied to cause oxygen evolution and hence acidification of the solution in the vicinity of the wire tips. Such highly acid solution would cause dissolution of contaminated oxide and carbonate films on a surface; the concomitant gas evolution would increase the effectiveness of the device through its stirring and scrubbing action. The technique would be particularly effective in the cleanup and decontamination of hard-to-reach areas, e.g., inside pipes, bends, joints, etc. The plausibility of the second idea can be surmised from the findings of Sturchio et al. [52] that U(IV) could substitute for Ca^{2+} in lattice vacancies of calcite ($CaCO_3$). The relative insolubility of calcite makes it a good host for the long-term storage of radionuclides such as U, Sr, lanthanides, and actinides. It might be mentioned that in Pamukale, Turkey, mountains of calcite deposit have resulted from the evaporation of mineral water containing a high concentration of Ca salts. Solar evaporation of dilute solutions of radionuclides in hard water could constitute a simple and cost-effective method of disposal and storage.

The present work, being a basic research project, was focused on seeking fundamental knowledge and unfortunately left little room for developing the above ideas. It can only be

hoped that these ideas will generate enough interest in others and become the subject of further work.

FEEDBACK

This Environmental Management Science Program is an excellent beginning in a national effort to apply scientific principles towards the solution of the world-wide problem of environmental pollution and degradation. It is unfortunate that funding of projects is generally short-lived, i.e., 3 years or less. Environmental problems are going to be with us as long as humans exist on this planet. They will continue to get worse as the world's population grows. A longer term scientific research effort to find solutions to these problems is needed. It is imperative that there be a national Basic Environmental Management Science Program that will fund basic research programs over 10 to 20 years. A similar program has been established by DOE in materials science and has had great success. Why not one in environmental science? This area should be a matter of national priority which DOE should vigorously pursue.

REFERENCES

1). R.P. Allen and H.W. Arrowsmith, Materials Performance **18**, 216 (1979).

2). T.W. Capehart, D.A. Corrigan, R.S. Lonell, K.I. Pandya, and R.W. Hoffman, App. Phys. Lett. **51**, 865 (1991).

3). Y.D. Chen and R. N. Noufi, J. Electrochem. Soc. **131**, 1447 (1984).

4). V. Markovac and M. Cohen, J. Electrochem. Soc. **114**, 678 (1967).

5). C.A. Melendres and A. Tadjeddine (eds), Synchrotron Techniques in Interfacial Electrochemistry, NATO ASI Series C, Kluwer Academic Publishers, Dordrecht, the Netherlands, **432** (1994).

6). C. A. Melendres and A. N. Mansour, Electrochim. Acta **43**, 631 (1997).

7). G.E. Brown Jr., G.A. Parks, and C.J. Chisholm-Brause, Chimia **43**, 248 (1989).

8). M. Balasubramanian, C. A. Melendres, and A. N. Mansour, J. Electrochem. Soc. **146**, 607 (1999).

9). A.N. Mansour, C.A. Melendres, M. Pankuch, and R.A. Brizzolara, J. Electrochem. Soc. **141**, L69 (1994).

10). A.N. Mansour and C.A. Melendres, Physica B **208** & **209**, 583 (1995).

11). S.I. Zabinsky, J.J. Rehr, A. Ankudinov, R.C. Albers, and M.J. Eller, Phys. Rev. B, **52**, 2995 (1995).

12). D.M. Pfund, J.G. Darab, J.L. Fulton, and Y. Ma, J. Phys. Chem**. 98**, 13102 (1994).

13). F. Mansfeld, Y. Wang, and H. Shih, J. Electrochem. Soc. **138**, L74 (1991).

14). A.J. Davenport, H.S. Isaacs, and M.W. Kendig, Corrosion Sci. **32**, 653 (1991).

15). L. E. Eary and D. Rai, Environ. Sci. Technol. **22**, 972 (1988).

16). A. F. White, in Mineral-Water Interface Geochemistry , M. F. Hochella, and A. F. White (eds.), Mineralogical Society of America, Washington, DC, pp. 468-505 (1990).

17). Edited by M. Reinhard and P. G. Tratnyek, Preprints of Papers: Contaminant Remediation of Zero-valent Metals, 209th ACS National Meeting, Anaheim, CA, American Chemical Society, Washington, DC, **18**, pp. 689-835 (1995).

18). J.A. Bardwell, G.I. Sproule, B. Macdougall, M. J. Graham, A. J. Davenport, and H. S. Isaacs, J. Electrochem. Soc. **139**, 371 (1992).

19). (a) K. I. Pandya, W. E. O'Grady, D.A. Corrigan, J. McBreen, and R. W. Hoffman, J. Phys. Chem. **94**, 21 (1990); (b) A. N. Mansour and C. A. Melendres, J. Phys. Chem A **102**, 65 (1998); (c) Y. Hu, I. T. Bae, Y. Mo, M. R. Antonio and D. A. Scherson, Can. J. Chem. **75**, 1721 (1997); (d) P. A. O'Day, G. E. Brown, Jr., and G. A. Parks, J. Colloid Interface Sci. **165**, 269 (1994).

20). M. L. Patterson, A. F. White, G. E. Brown, Jr., and G. A. Parks, Environ. Sci. Technol. **31**, 1573 (1997).

21). K. I. Pandya, Phys. Rev. B **50**, 15509 (1994).

22). A. F. Wells, in Structural Inorganic Chemistry, Fourth Edition, p. 520, Clarendon Press, Oxford (1975).

23). P. Axmann and O. Glemser, J. Alloys Comp. **246**, 232 (1997)

24). B. C. Cornilsen, X. Shan, and P. L. Loyselle, in Nickel Hydroxide Electrodes, D. A. Corrigan and A.H. Zimmerman (eds), PV **90-4**, p. 82, Electrochemical Society Proceedings Series, Pennington, NJ (1990).

25). C. Delmas, J. J. Braconnier, Y. Borthomieu, and P. Hagenmuller, Mat. Res. Bull. **22**, 741 (1987).

26). C. Delmas, C. Faure, L. Gautier, L. Guerlou-Demorgues, and A. Rougier, Phil. Trans. R. Soc. Lond. A **354**, 1545 (1996).

27). L. Demorgues-Guerlou, L. Fournes, and C. Delmas, J. Solid State Chem. **114**, 6 (1995).

28). D.A. Corrigan, T. W. Capehart, K.I. Pandya, and R.W. Hoffman, in Nickel Hydroxide Electrodes, D.A. Corrigan and A.H. Zimmerman, (eds), PV **90-4**, p. 97, Electrochemical Society Proceedings Series, Pennington, NJ (1990).

29). S. Kim, D.A. Tryk, M.R. Antonio, R. Carr, and D. Scherson, J. Phys. Chem. **98**, 10269 (1994).

30). K.I. Pandya, W.E. O'Grady, D.A. Corrigan, J. McBreen, and R.W. Hoffman, J. Phys. Chem **94**, 21 (1990).

31). C.A. Linkous, W.E. O'Grady, D. Sayers, and C. Y. Yang, Inorg. Chem. **25**, 3761 (1986).

32). J.H. Choy, D.H. Kim, and S.H. Hwang, J. Phys. IV (France) **7**, C1-337 (1997).

33). A.E. Bocquet, A. Fujimori, T. Mizokawa, T. Saitoh, H. Namatame, S. Suga, N. Kimizuka, Y. Takeda, and M. Takano, Phys. Rev. B **45**, 1561 (1992).

34). M. Abbate, F.M.F. de Groot, J.C. Fuggle, A. Fujimori, O. Strebel, F. Lopez, M. Domke, G. Kaindl, G.A. Sawatzky, M. Takano, Y. Takeda, H. Eisaki, and S. Uchida, Phys. Rev. B **46**, 4511 (1992).

35). J. Wong, F.W. Lytle, R.P. Messmer, and D.H. Maylotte, Phys. Rev. B **30**, 5596 (1984).

36). S.P.Cramer, T.K. Eccles, F.W. Kutzler, K.O. Hodgson, and L.E. Mortenson, J. Am. Chem. Soc. **98**, 1287 (1976).

37). K.I. Pandya, R.W. Hoffman, J.McBreen, and W.E. O'Grady, J. Electrochem. Soc. **137**, 383 (1990).

38). P.A. O'Day, J.J. Rehr, S.I. Zabinsky, and G.E. Brown. Jr., J. Am. Chem. Soc. **116**, 2938 (1994).

39). A. Manceau and J.M. Combes, Phys. Chem. Minerals **15**, 283 (1988).

40). J.M. Combes, A. Manceau, and G.J. Calas, Phys. Colloq. Paris **C8**, 697 (1986).

41). A. Szytula, A. Burewicz, Z. Dimitrijevic, S. Krasnicki, H. Rzany, J. Todorovic, A. Wanic, and W. Wolski, Phys. Status Solidi **26**, 429 (1968).

42). F.J. Ewing, J. Chem. Phys. **3**, 420 (1935).

43). A. Manceau and V.A. Drits, Clay Minerals 1993, **28**, 165 (1993).
44). M. Froment (ed.), Passivity of Metals and Semiconductors, Elsevier, Amsterdam (1983).
45). M. Kerkar, J. Robinson, and A.J. Forty, Faraday Discuss. Chem. Soc. **89**, 31 (1990).
46). P. G. Allen, D. Shuh, J. J. Bucher, N. M. Edelstein, C. Palmer, R. J. Siva, S. N. Nguyen, L. N. Marquez, and E. Hudson, Radiochimica Acta **75**, 47 (1996)
47). A. Bianconi, A. Marcelli, H. Dexpert, R. Karnatak, A. Kotani, T. Jo, and J. Petiau, Phys. Rev. B **35**, 806 (1987).
48). P. G. Allen et al., Inorg. Chem. **34**, 4797 (1995).
49). D. M. Giaquinta, L. Soderholm, S. E. Yuchs, and S. R. Wasserman, Radiochim. Acta **76**, 113 (1997).
50). H. A. Thompson, G. E. Brown, and G. A. Parks, Amer. Mineral. **82**, 483 (1997).
51). Private communications with R.P. Allen, Pacific Northwest National Laboratory, and D.B. Chamberlain, Argonne National Laboratory, 1996.
52). N.C. Sturchio, M.R. Antonio, L. Soderholm, S.R. Sutton, and J.C. Brannon, Science **281**, 971 (1998).

ACKNOWLEDGEMENT

This research was supported under Grant No. W-31-109-ENG-38, Environmental Management Science Program, Office of Science and Technology, Office of Environmental Management, U.S. Department of Energy (DOE). X-ray Absorption Spectroscopy measurements were carried out at the National Synchrotron Light Source (NSLS) in Upton, NY, at the Stanford Synchrotron Radiation Laboratory (SSRL) in Stanford, CA, and at the Advanced Photon Source (APS) in Argonne, IL. We thank Dr. Mike Sansone, for help in the operation of beamline X10C at the NSLS, Dr. Joe Woicik (beamline X23A2 at NSLS), Dr. Hal Thompkins (SSRL), Dr. Jennifer Linton (beamline 12 BM-B at APS), and Dr. Jeremy Kropf (beamline 10 ID-B at APS). All the foregoing beamlines and synchrotron facilities are supported by the Department of Energy, Office of Science. Dr. M. Balasubramanian did most of the XAS measurements and data analyses in this project and his contribution is gratefully acknowledged. Dr. George Meizner (Edge Analytical) assisted in carrying out preliminary XAS measurements on nickel oxides.

APPENDIX

Table I. Structural parameters for Ce compounds from EXAFS data analysis.

Sample	$r^{(Ce-Ce)}$ [Å]	$r^{(Ce-O)}$ [Å]	$\sigma^2_{(Ce-Ce)}$ [10^{-3} Å^2]	$\sigma^2_{(Ce-O)}$ [10^{-3} Å^2]
Ce(OH)	3.76 (2)	4.41 (2)	10.3 (7)	17.8 (3.3)
CeO_2	3.80 (1)	4.46 (1)	3.3 (3)	6.5 (1.3)
Ce-in-NiOOH Film	3.74 (2)	4.39 (3)	12.3 (9)	18.9 (308)
Anodically deposited cerium oxide film	3.73 (2)	4.38 (3)	11.9 (7)	16.8 (2.7)

Table II. Summary of the local structural parameters derived from EXAFS data analysis**.**

Sample	Δk [Å^{-1}]	Δr [Å]	Shell	σ^2 [10^{-3} Å^2]	r [Å]	ΔE_0 [eV]
$Fe(OH)_2$	3.0-13.0	1.30-3.45	Fe-O Fe-Fe	9.2 ± 1.2 14.5 ± 1.9	2.097 ± 0.008 3.196 ± 0.016	9.2 ± 0.8 7.1 ± 1.5
Fe-$Ni(OH)_2$ "in situ"	2.5-11.5	1.15-3.30	Fe-O Fe-Ni	5.8 ± 0.5 10.4 ± 0.6	2.001 ± 0.006 3.106 ± 0.011	10.6 ± 0.7 13.3 ± 1.4
Fe-$Ni(OH)_2$ "ex situ"	2.5-11.5	1.15-3.30	Fe-O Fe-Ni	4.6 ± 0.4 7.0 ± 0.3	2.003 ± 0.005 3.109 ± 0.008	10.8 ± 0.6 12.7 ± 1.1
Fe-NiOOH "in situ"	2.5-11.5	1.10-3.10	Fe-O Fe-Ni	7.9 ± 0.9 6.8 ± 0.5	1.941 ± 0.012 2.843 ± 0.010	12.3 ± 1.1 8.0 ± 1.4

The Fe EXAFS data were Fourier transformed over the k-range Δk and fitted over the r-range Δr to two single-scattering paths involving oxygen and metal (Fe/Ni) atoms. The many-body amplitude reduction factor was fixed at 0.78 (the value found by fitting the data of reference standards). In the initial fits the coordination number was varied for both shells. However, in all cases the coordination number turned out to be within ~20% of the value expected for the brucite structure (6). Hence, in the final fits the coordination number for both the Fe-O first neighbor shell and the Fe-metal second neighbor shell was fixed at 6, as required by the α-$Ni(OH)_2$, $Fe(OH)_2$, and γ-NiOOH crystal structures. The distance r, disorder σ^2, and inner potential shift ΔE_0 were varied for both the coordination shells.

Table III. Structural parameters derived from analysis of EXAFS data for uranium in various samples.

Sample	Shell		r [Å]	σ^2 [10^{-3} Å^2]
U(VI) in solution	U-O $_{axial}$	2	1.776 ± 0.005	1.63 ± 0.35
	U-O $_{equ}$	6.00 ± 1.00	2.414 ± 0.012	8.97 ± 1.90
Pure U(VI) film "in situ"	U-O $_{axial}$	1.46 ± 0.32	1.838 ± 0.012	1.50 ± 1.20
	U-O $_{equ1}$	3.96 ± 1.50	2.280 ± 0.028	7.20 ± 3.00
	U-O $_{equ2}$	2.39 ± 0.83	2.467 ± 0.047	7.20 ± 3.00
U(VI)+$Ni(OH)_2$ "in situ"	U-O $_{axial}$	1.92 ± 0.12	1.822 ± 0.004	1.99 ± 0.37
	U-O $_{equ1}$	2.76 ± 0.47	2.304 ± 0.014	6.44 ± 1.73
	U-O $_{equ2}$	2.62 ± 0.83	2.473 ± 0.016	6.44 ± 1.73
U(VI)+$Ni(OH)_2$ "ex situ"	U-O $_{axial}$	1.98 ± 0.20	1.825 ± 0.007	2.22 ± 0.68
	U-O $_{equ1}$	2.41 ± 0.63	2.298 ± 0.016	4.50 ± 2.07
	U-O $_{equ2}$	2.51 ± 0.55	2.469 ± 0.018	4.50 ± 2.07

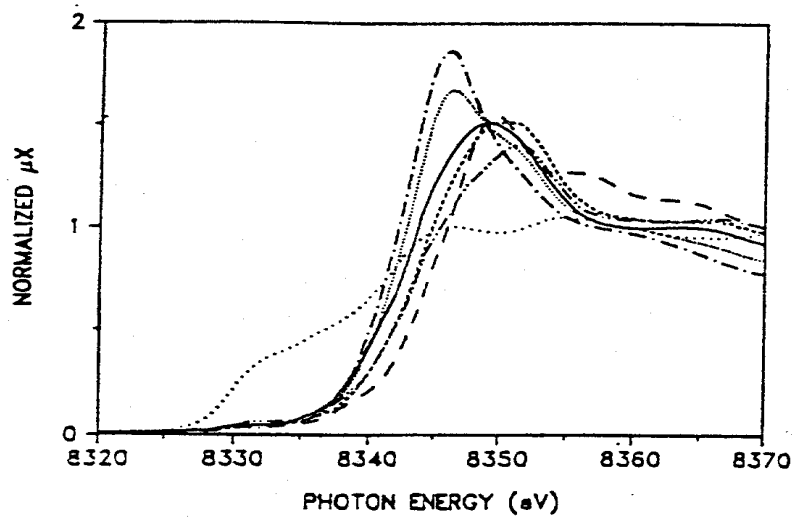

Figure 1. X-ray absorption near-edge structure (XANES) of the Ni K-edge for electrodeposited nickel oxide film and other reference materials. (....) Ni, (-.-) $NiSO_4$ in solution ,(. . .) nickel oxide electrodeposited from sulfate solution at 1.10 V vs. SCE , (---) electro-deposited nickel oxide charged at 0.5 V in 1 M KOH solution,(__) β-NiOOH, (-..-) γ-NiOOH (chemically prepared), (- -) $KNiIO_6$.

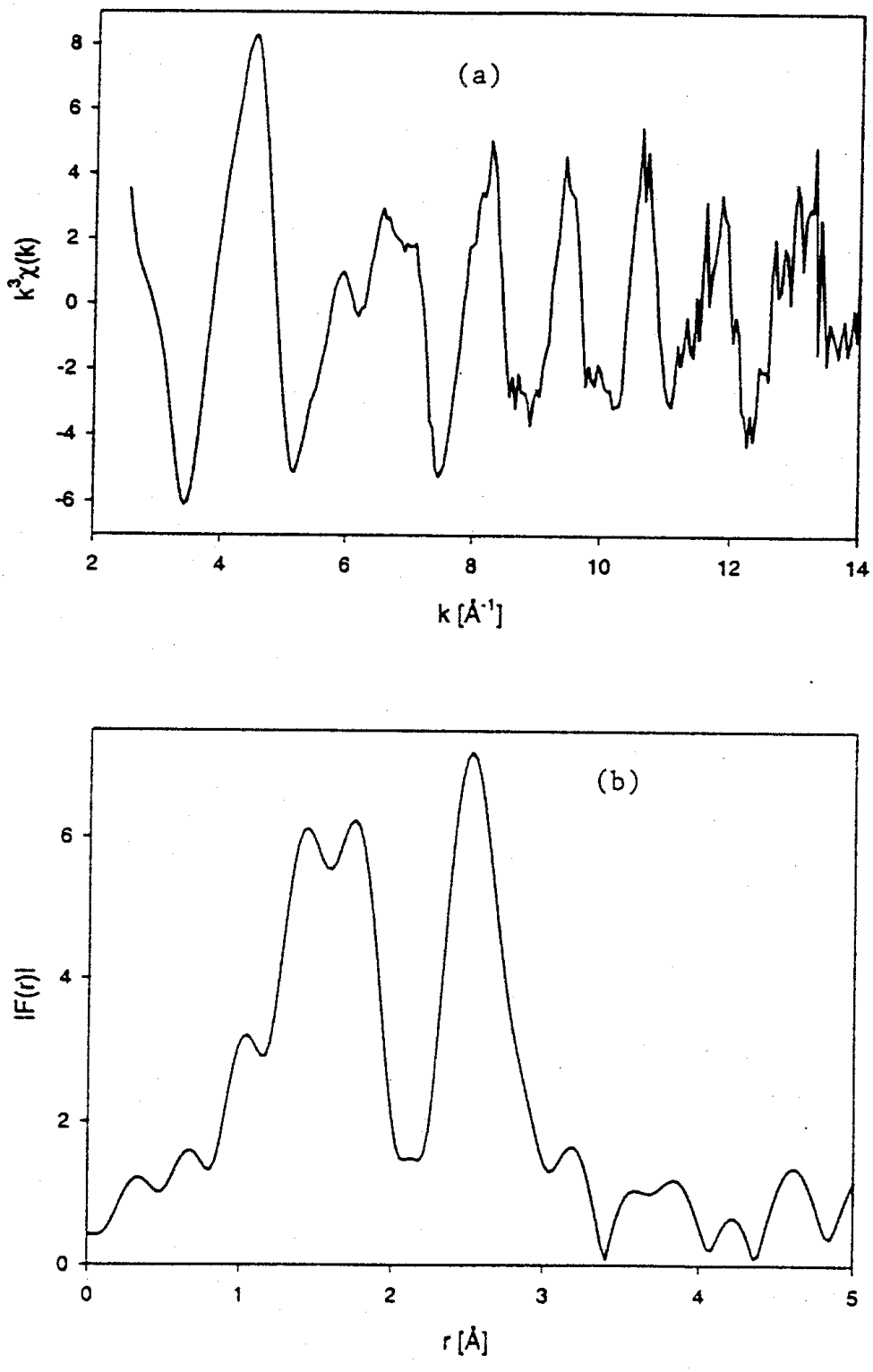

Figure 2 (a) k^3-weighted EXAFS function for NiOOH film electrodeposited at 1.10 V vs. SCE from a $NiSO_4$, solution. (b) Corresponding k^3-weighted Fourier transform.

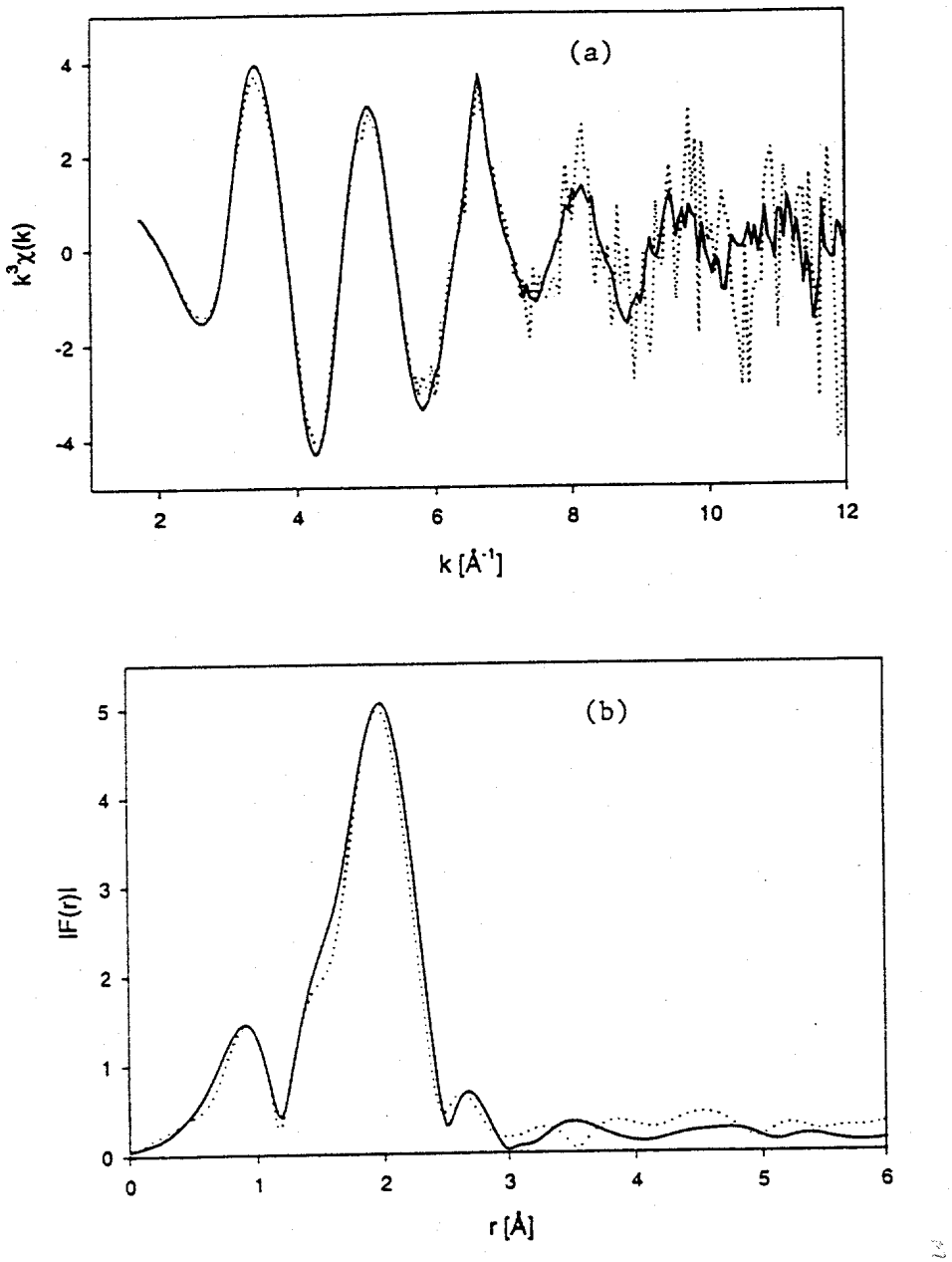

Figure 3. (a) Comparison of Sr K-edge EXAFS function for Sr^{2+} incorporated into cathodically deposited α-$Ni(OH)_2$ film (....) and for Sr^{2+} in a 0.1 M strontium acetate solution (__). (b) Corresponding k^3-weighted Fourier transform.

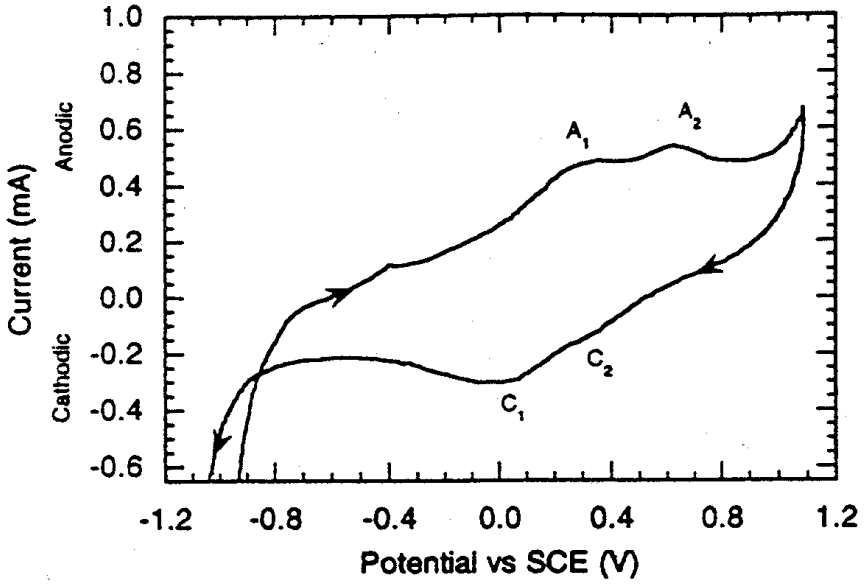

Figure 4. Cyclic voltammogram at a graphite electrode in 0.04 M Ce(III) acetate + 0.05 M $NiSO_4$+ 0.5 M sodium acetate; scan rate = 10 mV/sec.

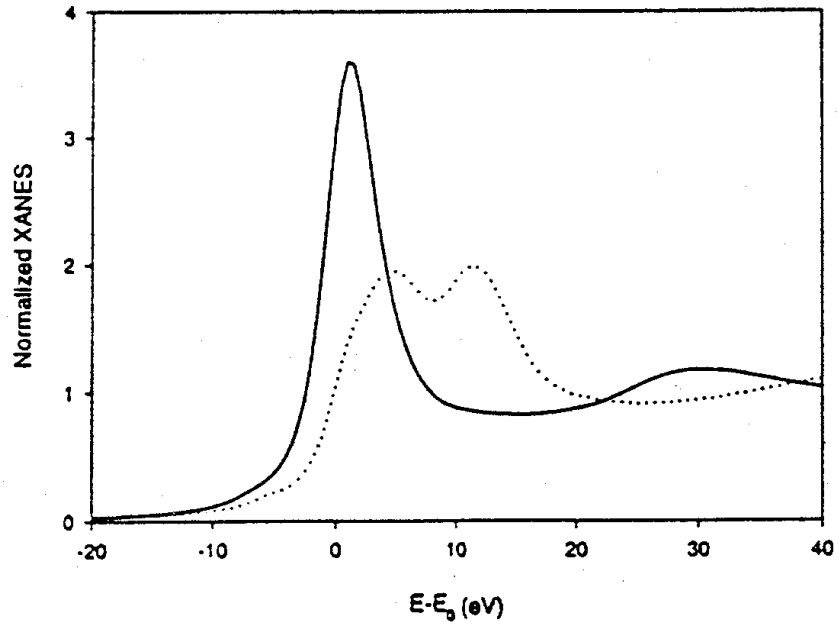

Figure 5. XANES spectrum of Ce(III) in a standard sample of cerium acetate (__) and of Ce(IV) in $Ce(OH)_4$ reference (....); both spectra taken in transmission.

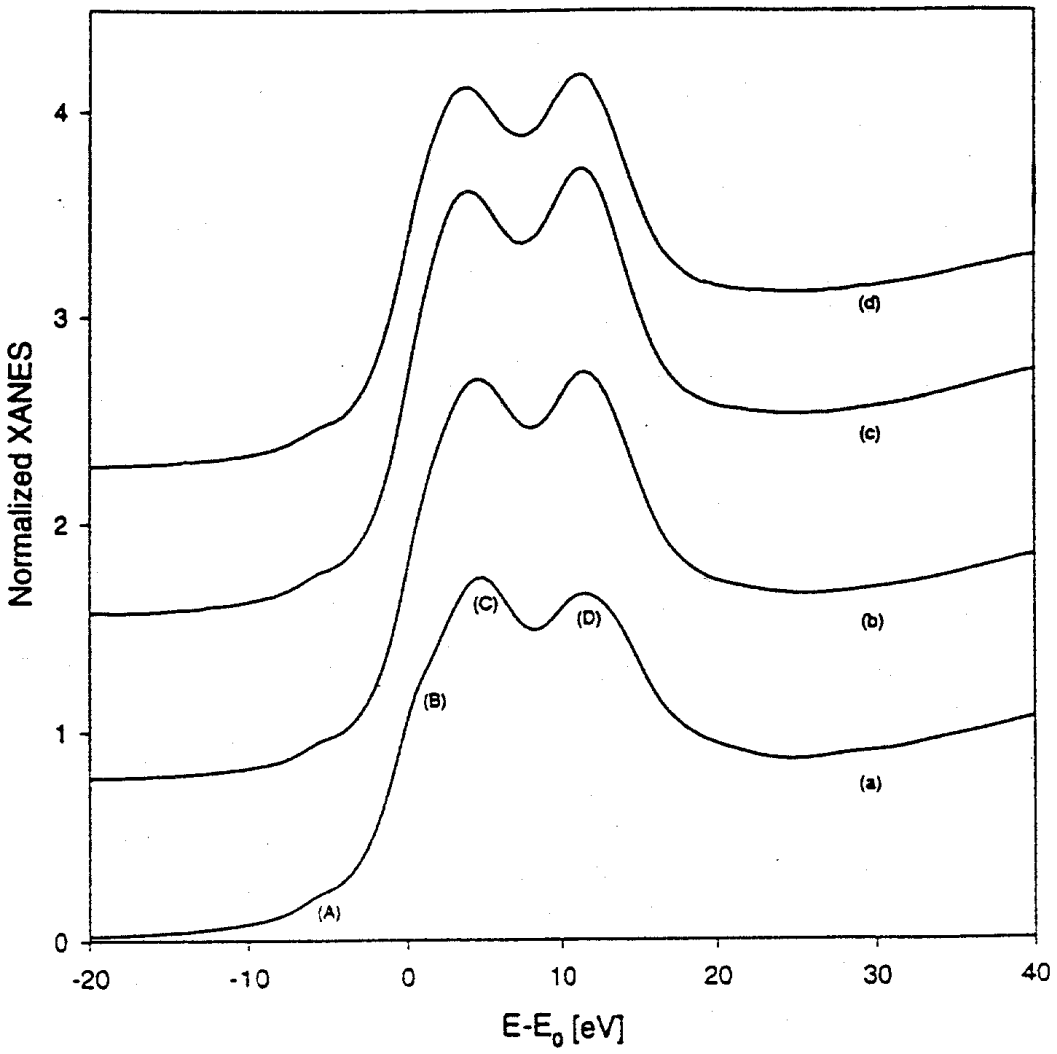

Figure 6. XANES spectra of Ce at the L(III) edge.
(a) CeO_2 standard
(b) $Ce(OH)_4$ reference
(c) Ce co-deposited with NiOOH film
(d) Ce anodically codeposited from a 0.08 M Ce(III) acetate solution

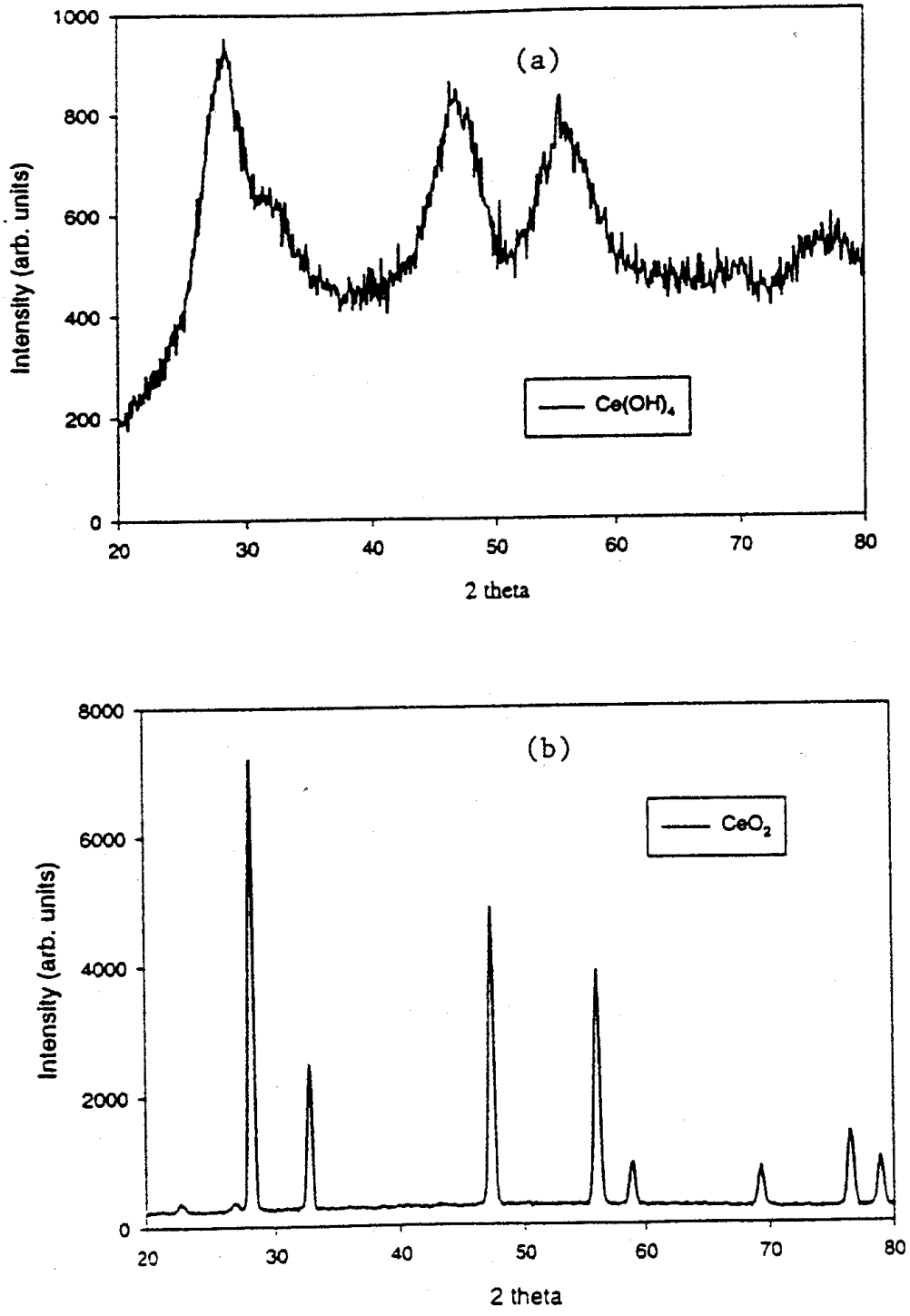

Figure 7. X-ray diffraction patterns of reference compounds (a) $Ce(OH)_4$ and (b) CeO_2

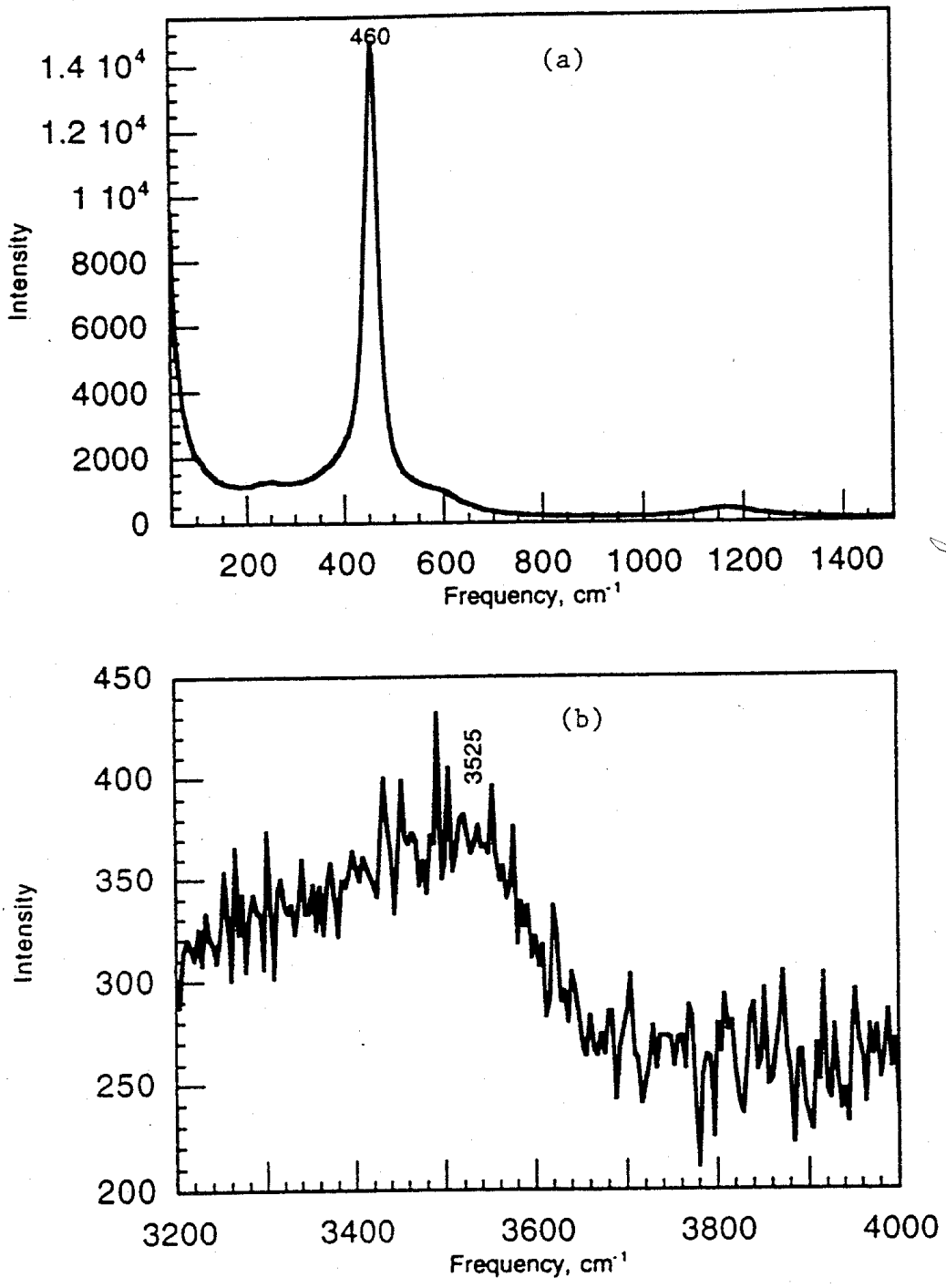

Figure 8. Laser Raman spectra of $Ce(OH)_4$ in KBr pellet; Ar^+ laser, 514.5 nm line, power ~25 mW (a) and 110 mW (b).

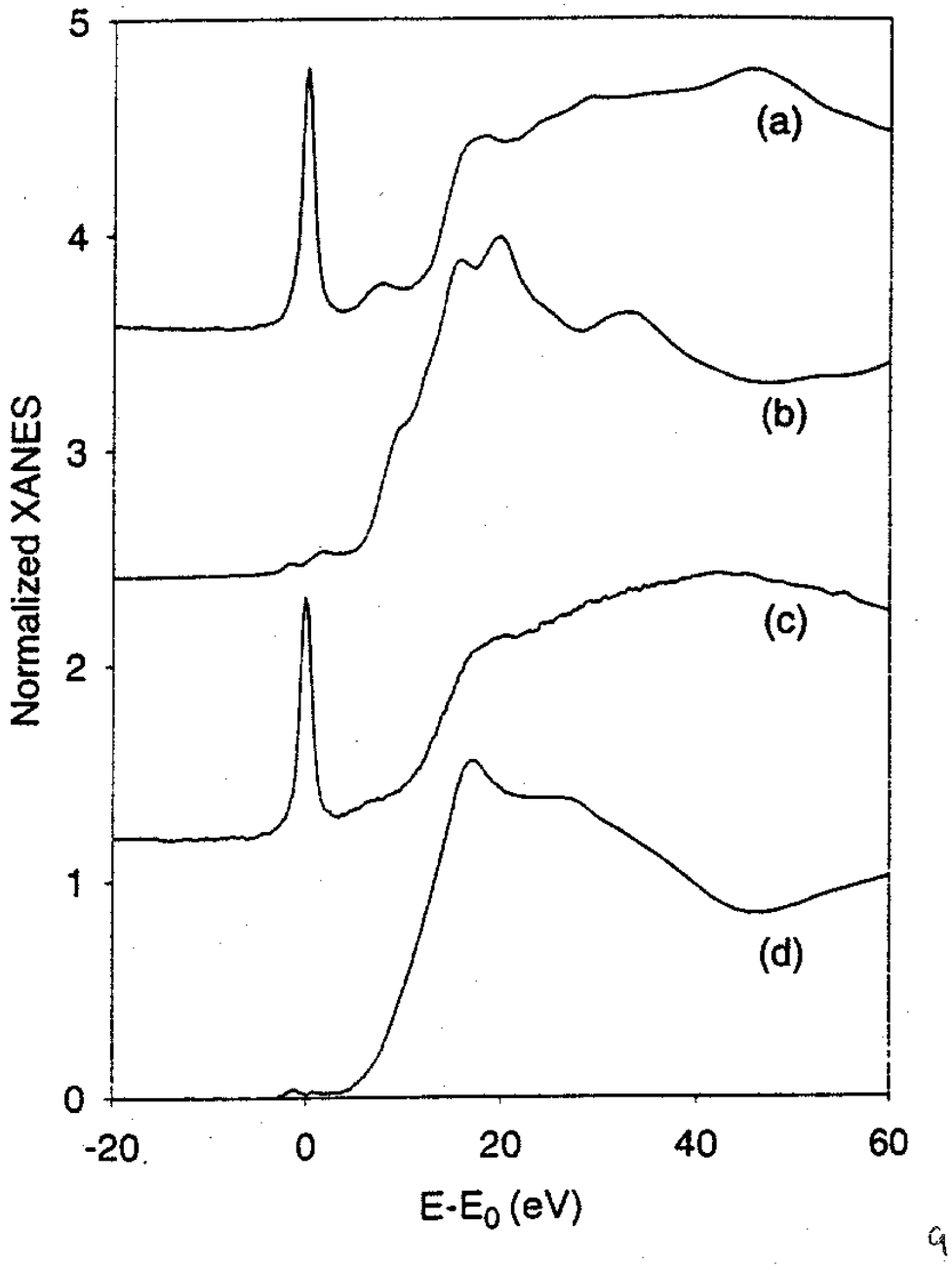

Figure 9. Chromium XANES of (a) K_2CrO_4, (b) Cr_2O_3, (c) Cr^{6+} in 0.5 M K_2CrO_4 solution, and (d) Cr^{3+} in 0.5 M $Cr(NO_3)_3$ solution

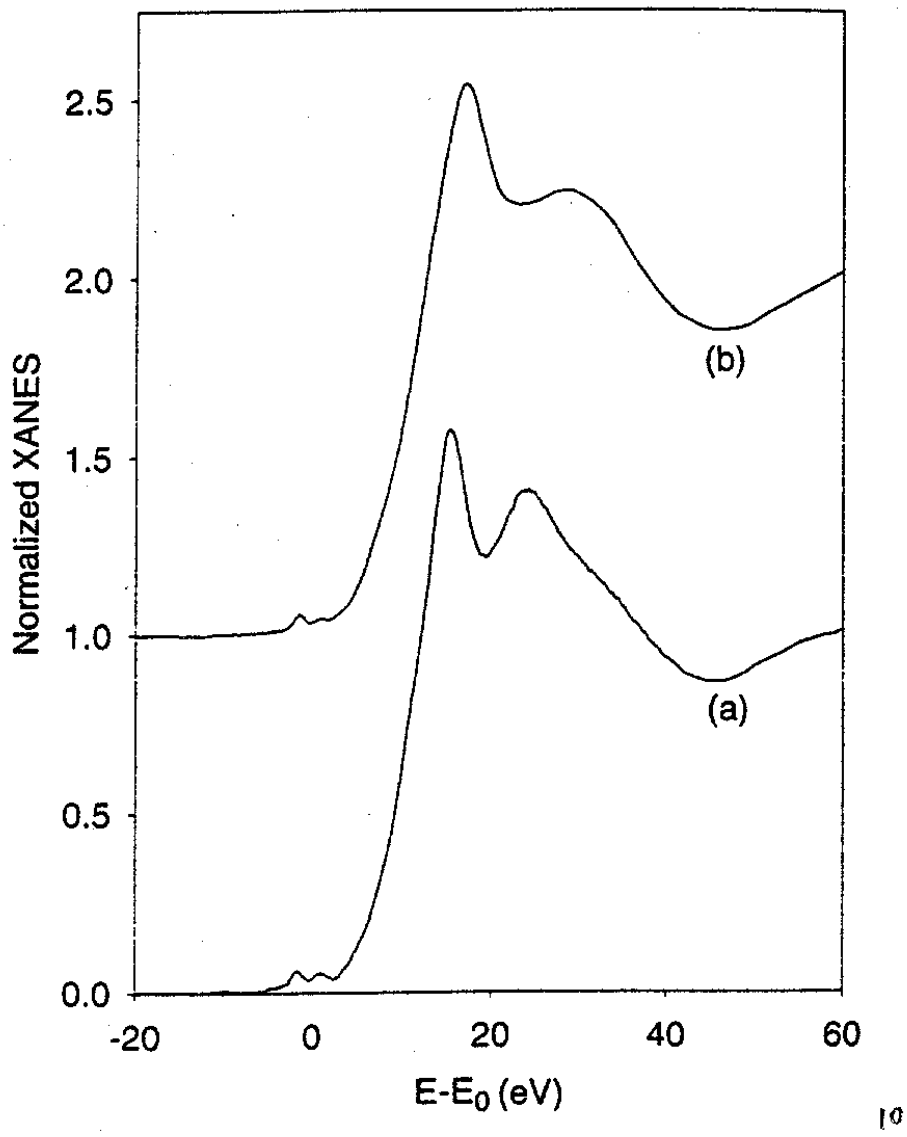

Figure 10. "In situ" Chromium XANES of cathodically deposited film from (a) 0.01 M $Cr(NO_3)_3$ and (b) 0.01 M $Cr(NO_3)_3$ + 0.1 M $Ni(NO_3)_2$.

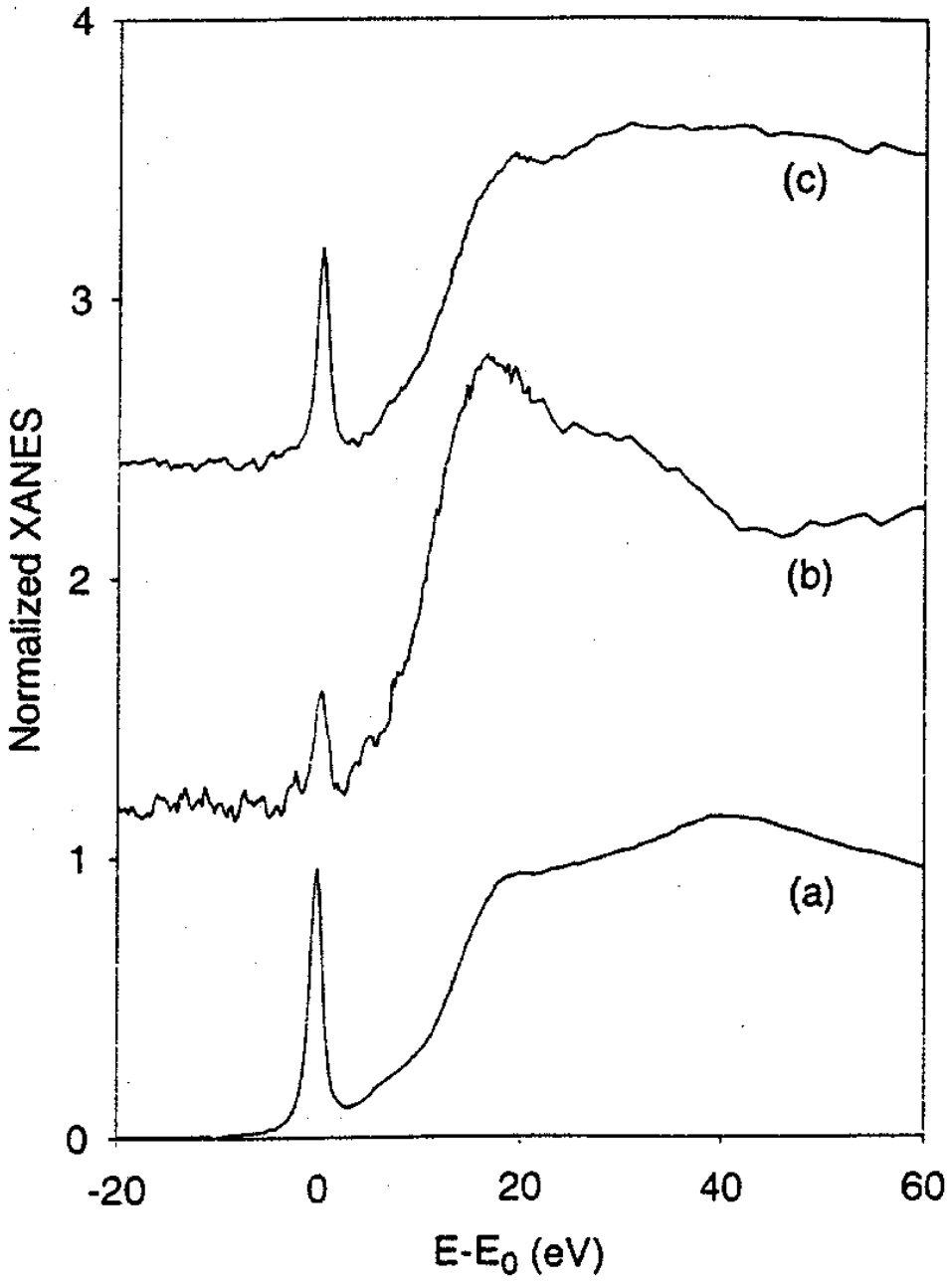

Figure 11. Chromium XANES of cathodically deposited film from (a) 0.01 M K_2CrO_4 + 0.1 M $Ni(NO_3)_2$ measured "in situ", (b) 0.01 M K_2CrO_4 measured "in situ", and (c) 0.01 M K_2CrO_4 measured "ex situ".

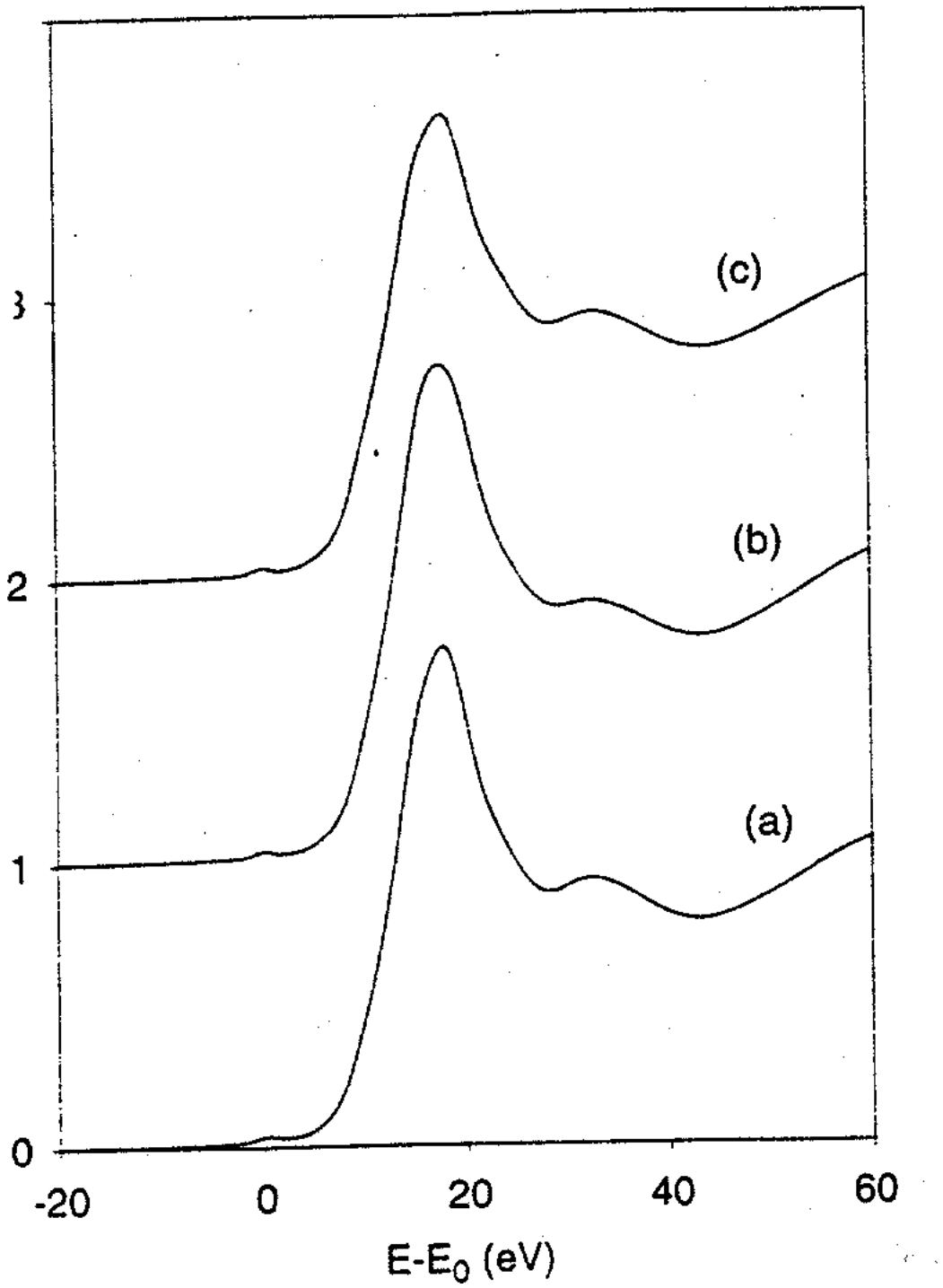

Figure 12. "Ex situ" Nickel XANES of cathodically deposited film from (a) 0.1 M $Ni(NO_3)_2$, (b) 0.01 M $Cr(NO_3)_3$ + 0.1 M $Ni(NO_3)_2$, and (c) 0.01 M K_2CrO_4 + 0.1 M $Ni(NO_3)_2$.

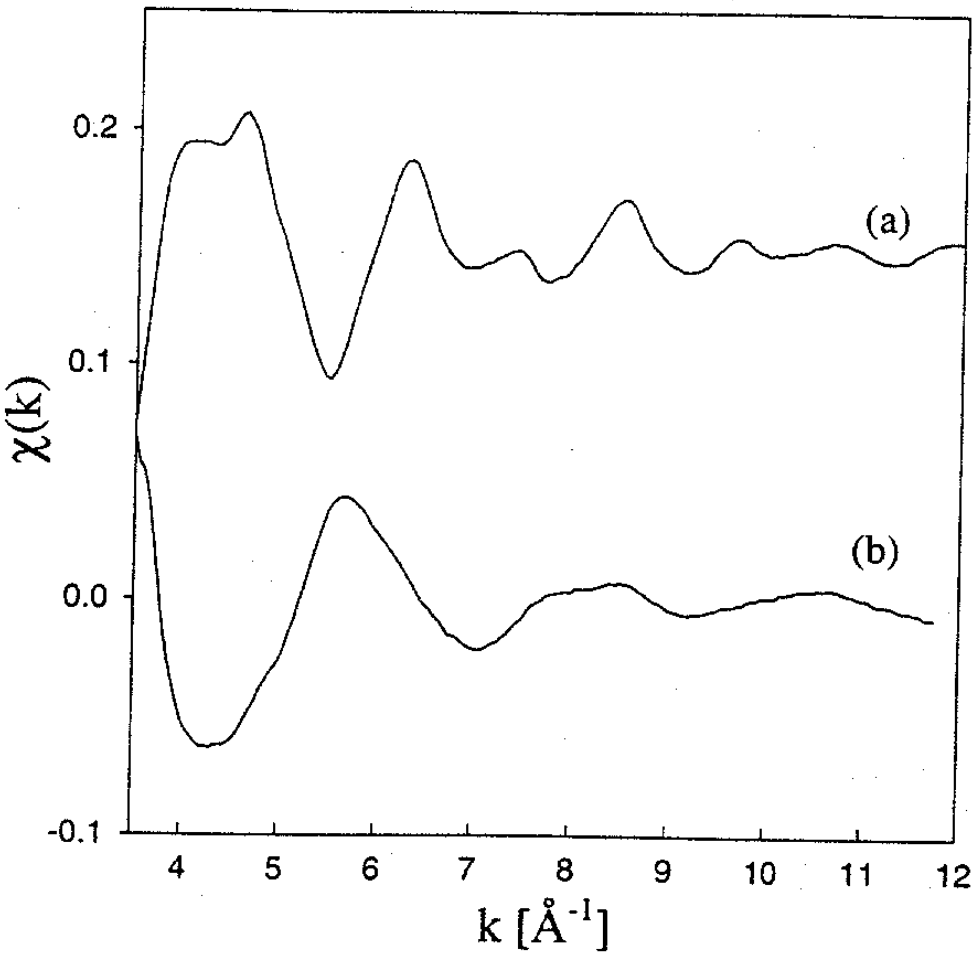

Figure 13. EXAFS spectra of Cr absorbers in (a) Sample I and (b) Sample II.

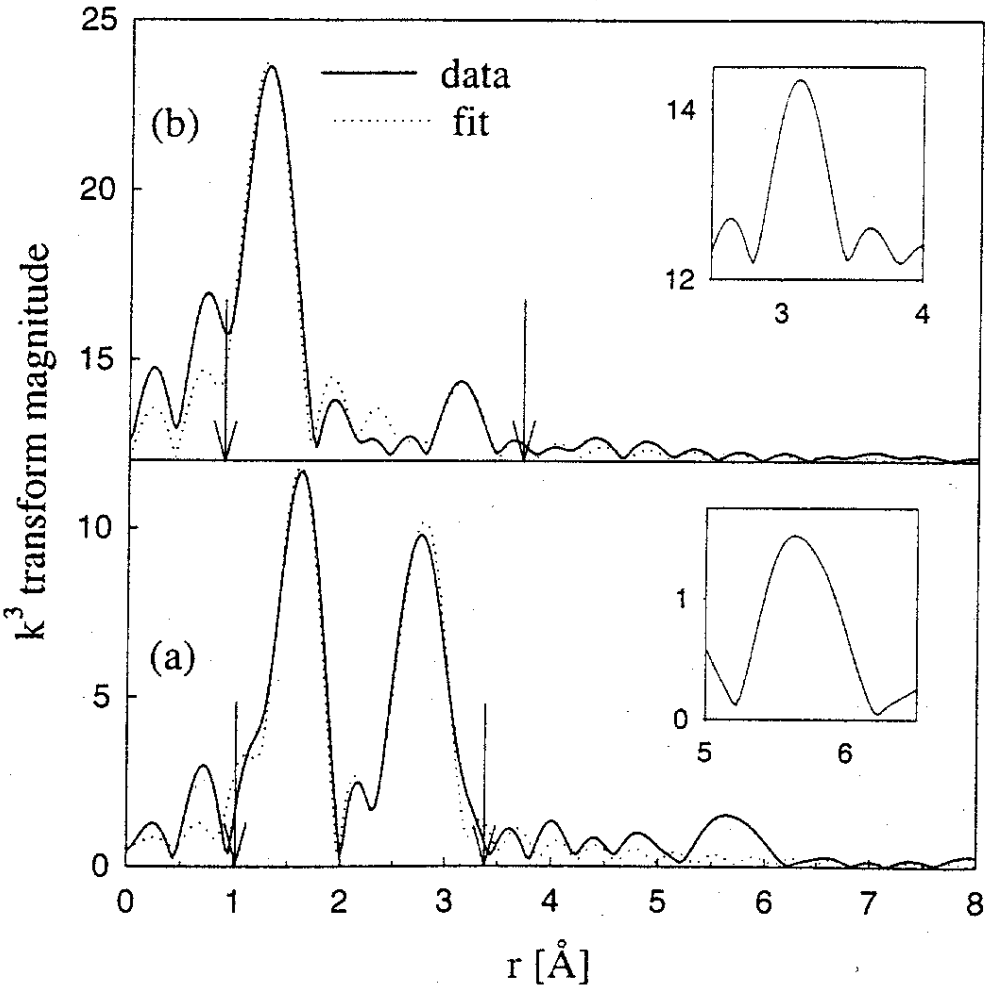

Figure 14. Fourier transform of Cr absorbers in (a) Sample I and (b) Sample II. The fits to the data obtained are also illustrated. The arrows indicate the fitting range covered. Small peaks of relevance are enlarged and shown in the insets.

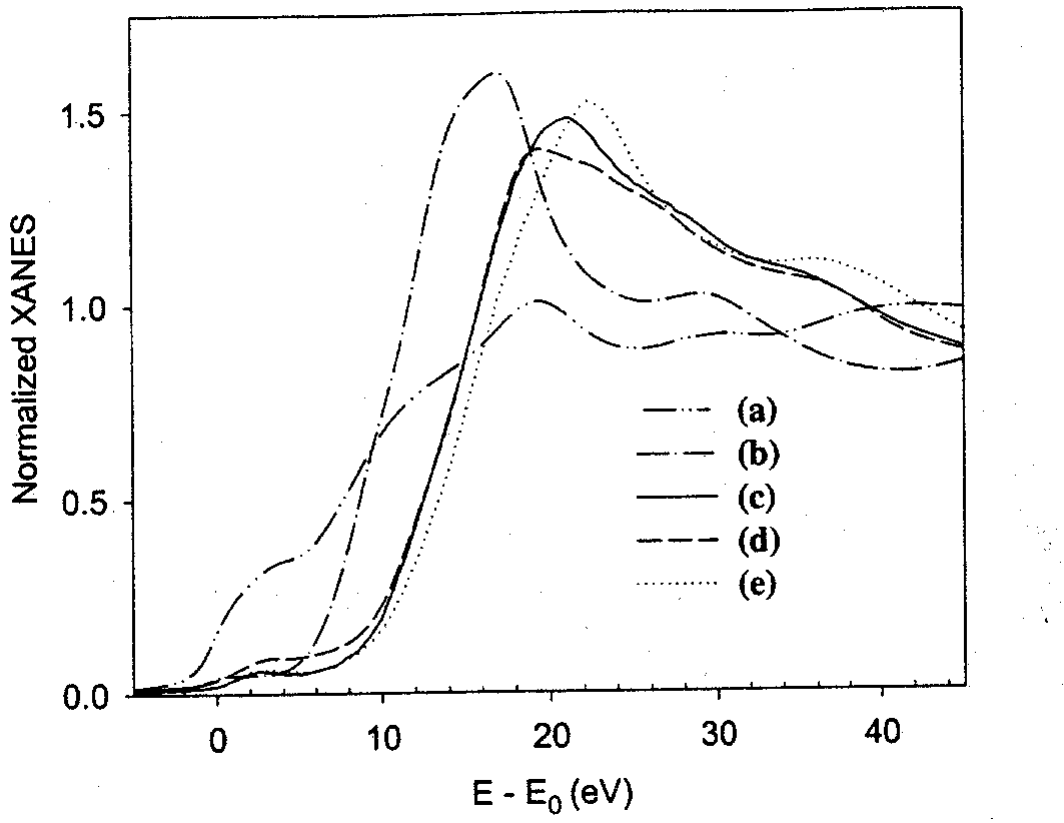

Figure 15. K-edge XANES of Fe absorbers in (a) α-Fe, (b) chemically prepared $Fe(OH)_2$, (c) Fe in α-$Ni(OH)_2$, (d) α-FeOOH, and (e) Fe in γ-NiOOH.

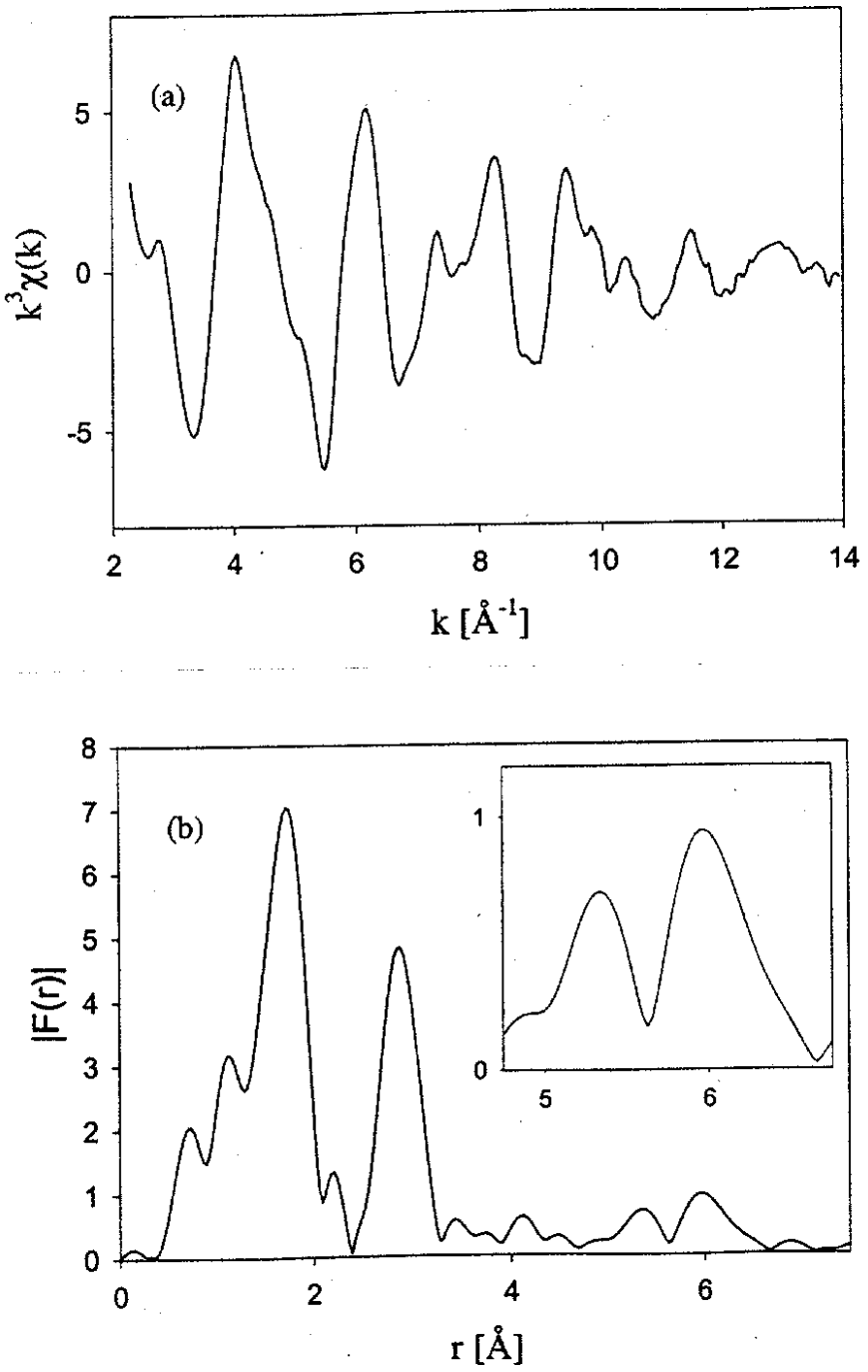

Figure 16. (a) K-edge EXAFS $\chi(k)$ function of Fe absorbers in chemically prepared $Fe(OH)_2$ and (b) corresponding Fourier transform (small peaks of relevance are enlarged in the inset).

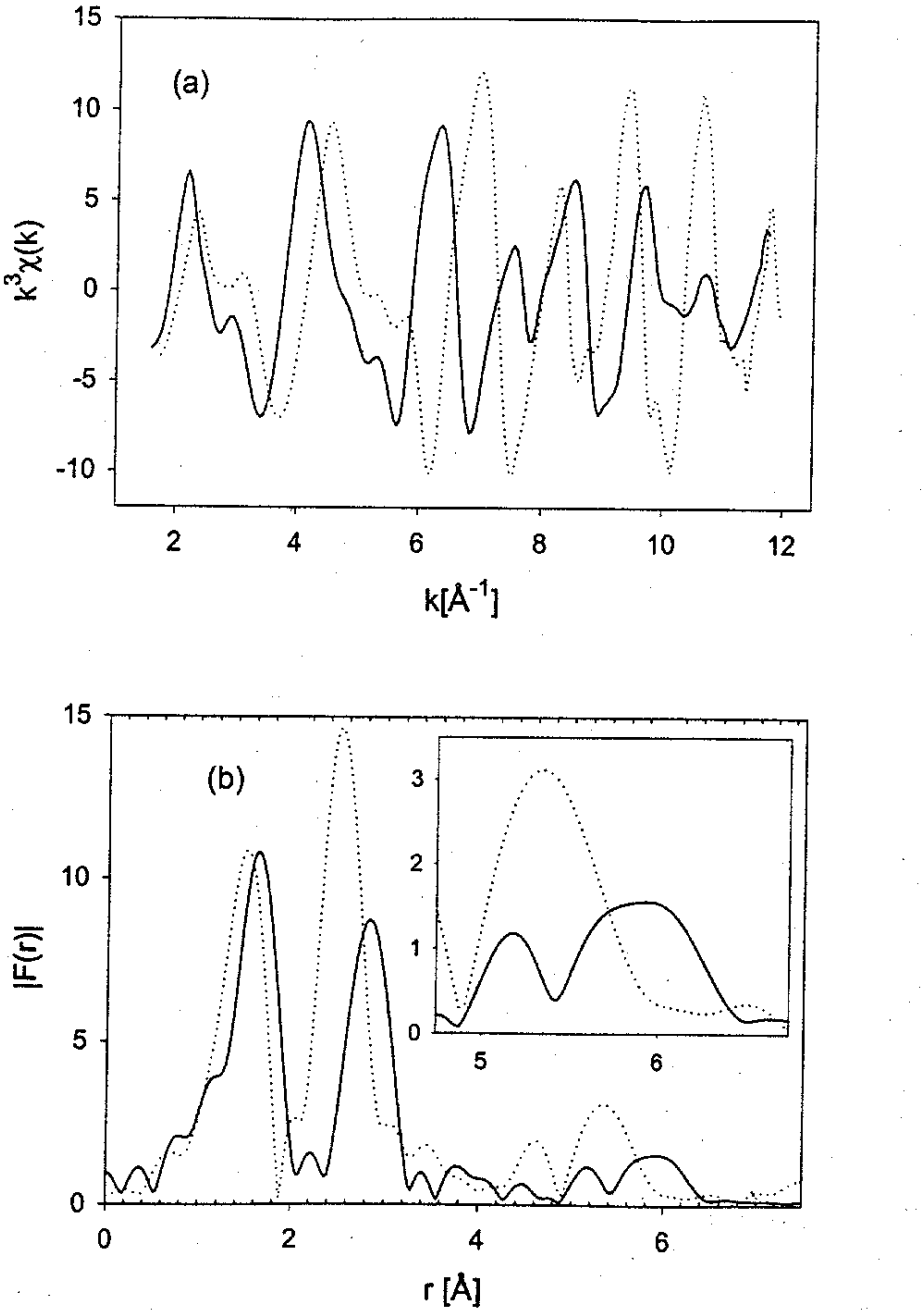

Figure 17. (a) K-edge EXAFS $\chi(k)$ function of Ni absorbers in α-$Ni(OH)_2$ (solid) compared with γ-NiOOH (dotted), and (b) corresponding Fourier transforms (small peaks of relevance are enlarged in the inset).

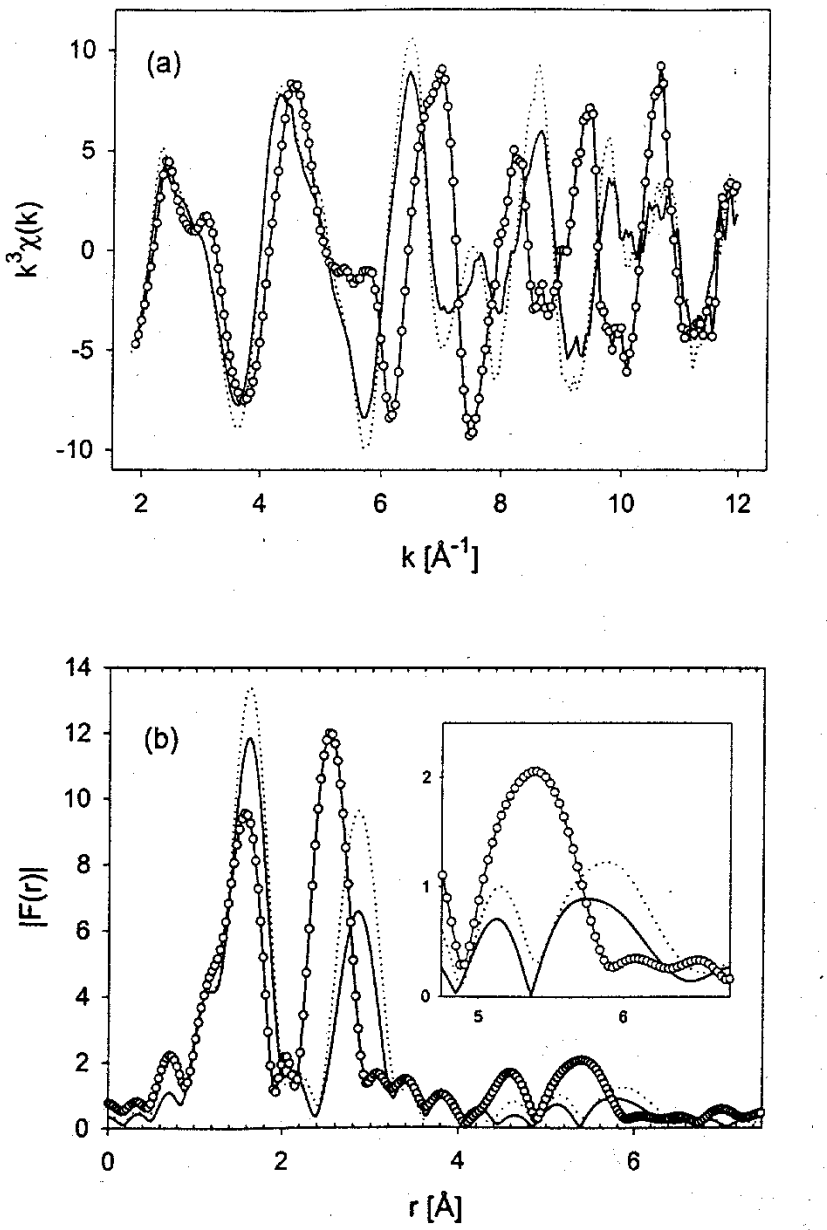

Figure 18. (a) EXAFS $\chi(k)$ function of Fe in α-$Ni(OH)_2$ obtained "in situ" (solid) and "ex-situ" (dotted) compared with Fe in γ-NiOOH (circles) and (b) corresponding Fourier transforms (small peaks of relevance are enlarged in the inset).

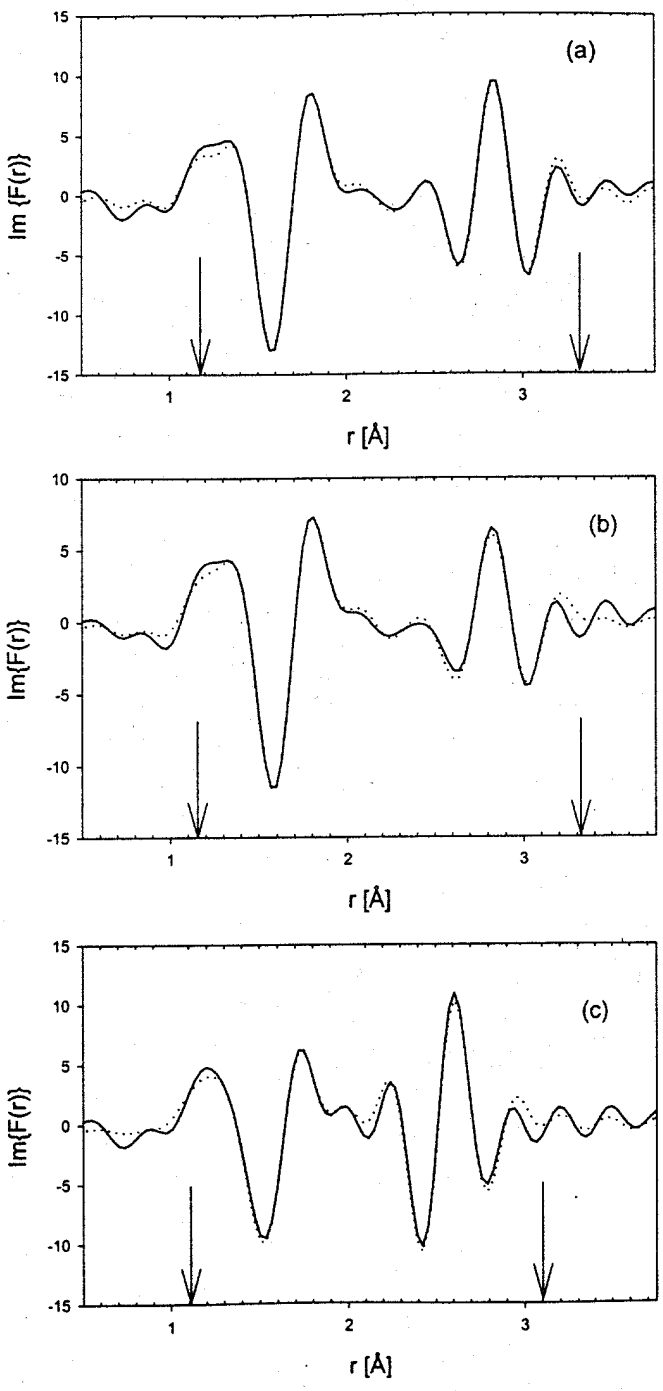

Figure 19. Fits to EXAFS of Fe absorbers in (a) α-$Ni(OH)_2$ ("ex situ"), (b) α-$Ni(OH)_2$ ("in-situ"), and (c) γ-NiOOH. All fits (dotted) are compared to experimental data (solid). The arrows indicate the r-range over which the fits were performed.

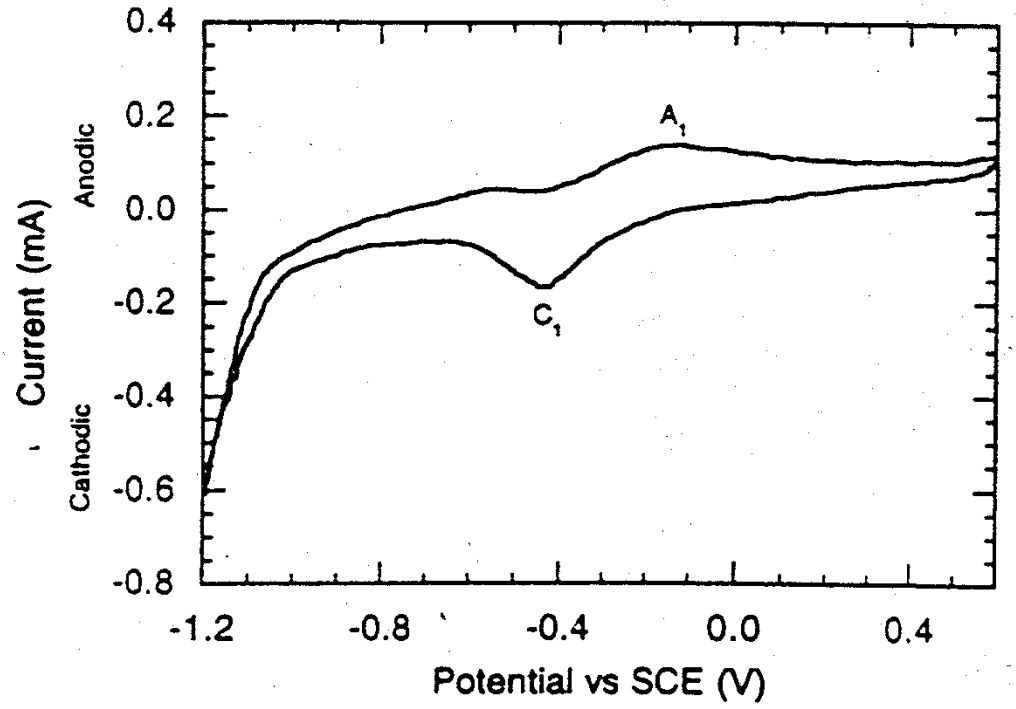

Figure 20. Cyclic voltammogram of graphite in deaerated 0.005 M $FeSO_4$ + 0.3 M H_3BO_3 + 0.075 M $Na_2B_4O_7$ solution; scan rate = 10 mV/sec.

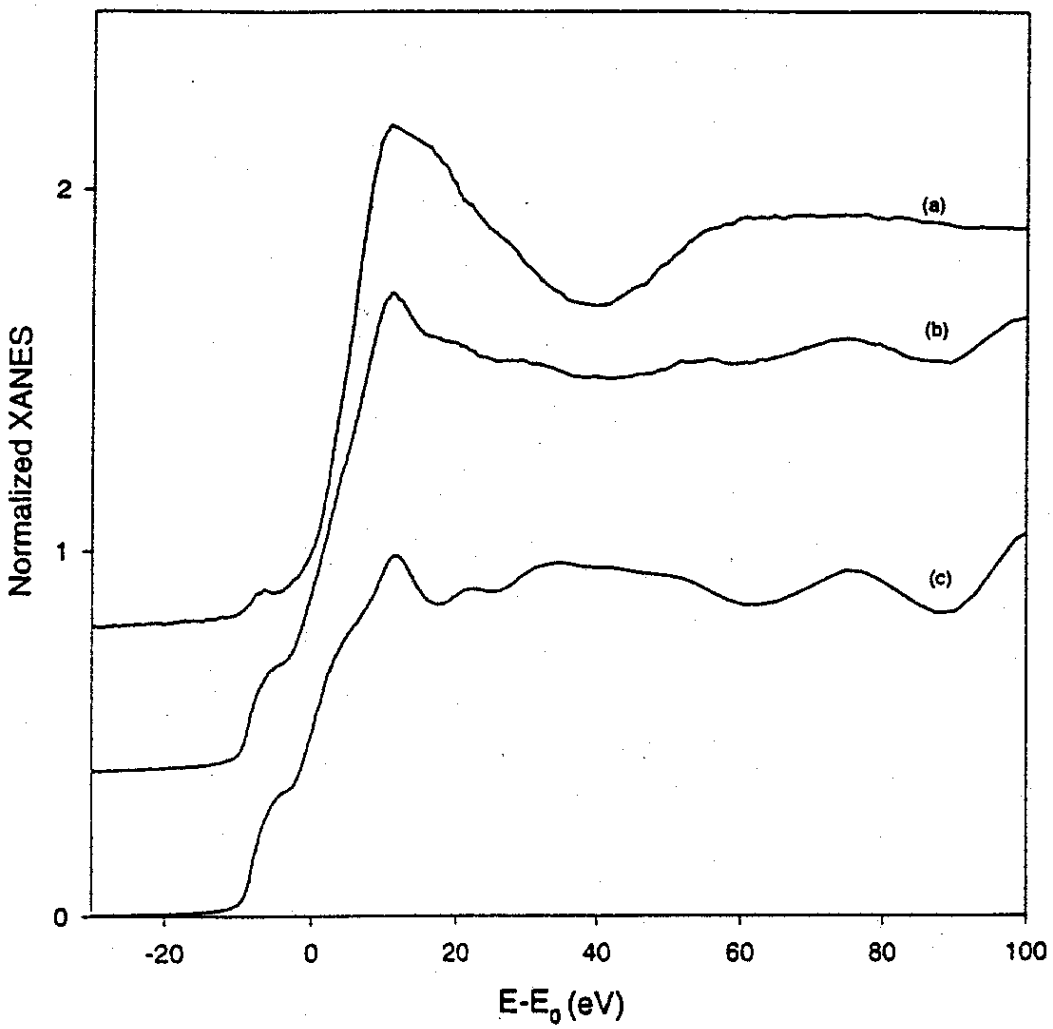

Figure 21. Iron K-edge XANES spectra in (a) anodically deposited film at 0.6 V, (b) film cathodically reduced at – 1.05 V, and (c) iron foil reference.

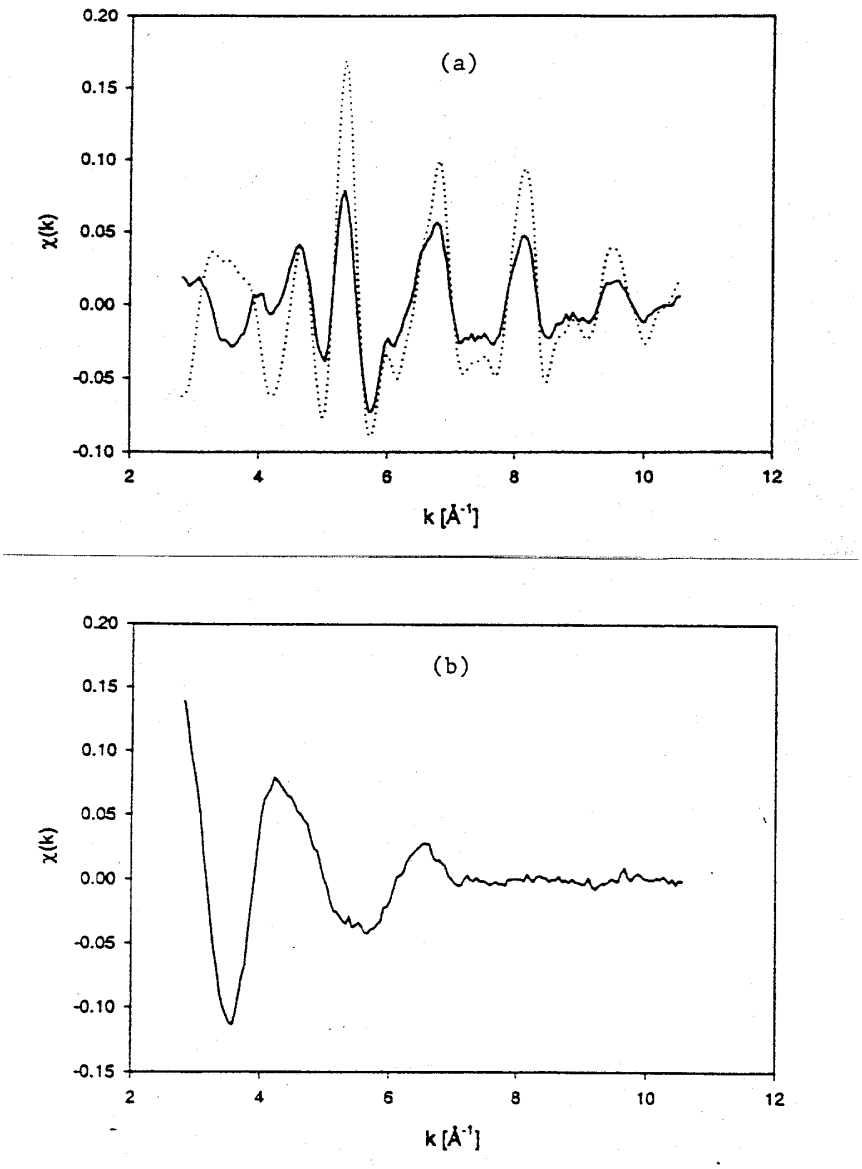

Figure 22. Iron K-edge EXAFS for a iron foil reference taken at (a) 80 K (....), and cathodically reduced film at -1.05 V (__), and (b) anodically formed film at 0.6 V.

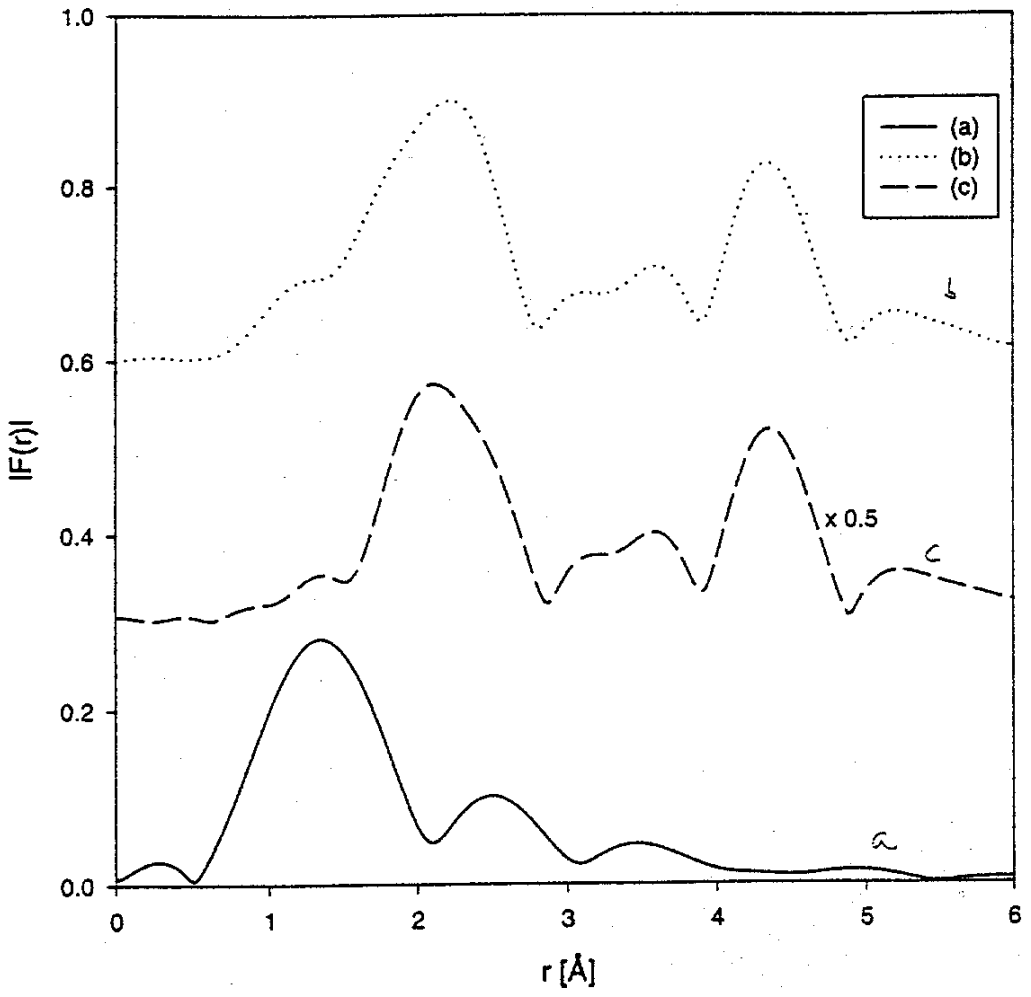

Figure 23. Fourier Transform (k-weighted) of: (a) anodically deposited iron oxide film at 0.6 V, (b) iron foil reference (spectrum taken at -80 K), and (c) film cathodically reduced at -1.05 V.

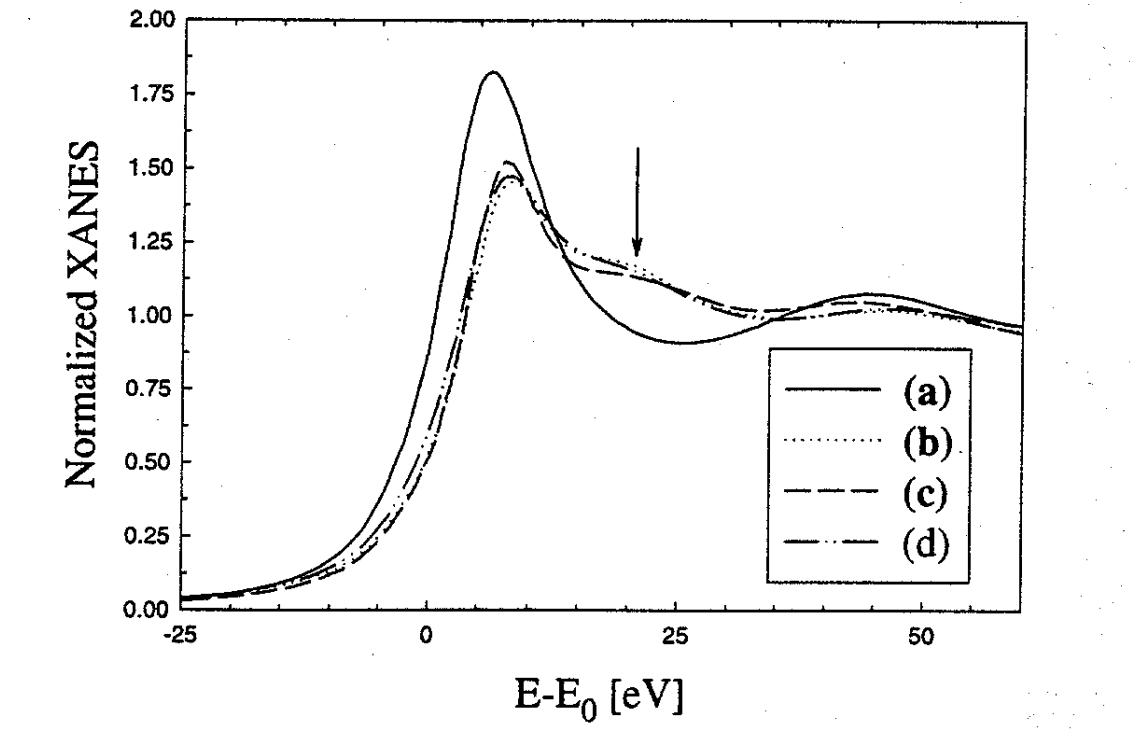

Figure 24. U-L(III) edge XANES spectra for (a) U(IV) solution prepared by reduction of U(VI) nitrate with rongalite, (b) U(VI) + $Ni(OH)_2$ "in-situ", (c) U(VI) nitrate solution, and (d) pure U(VI) cathodically deposited film, "in-situ".

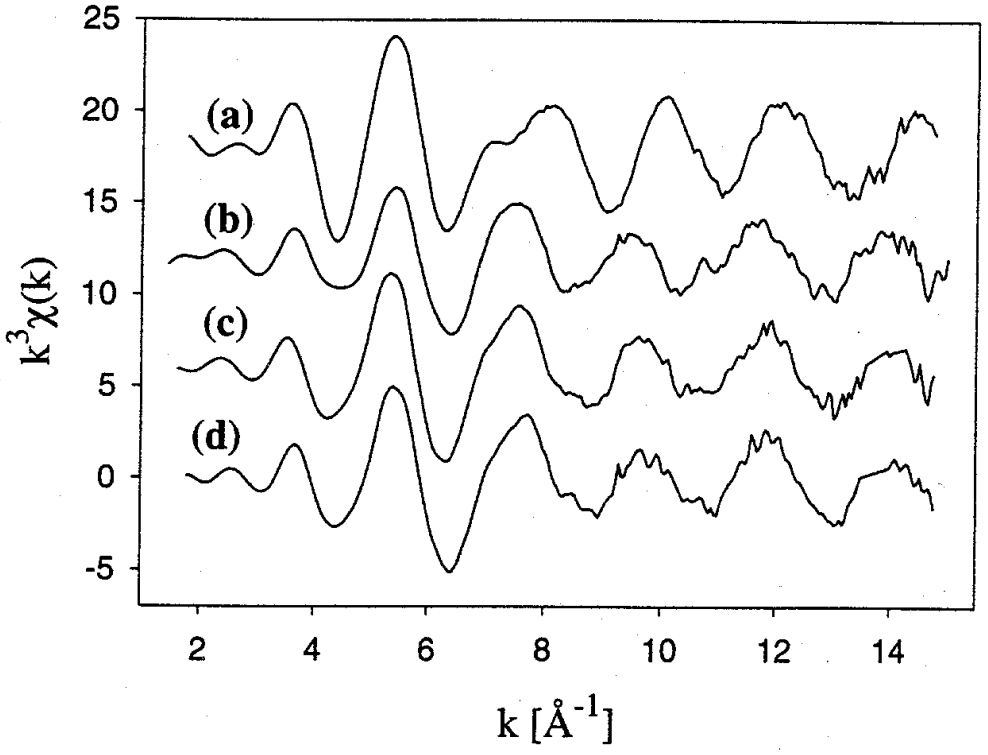

Figure 25. k^3-weighted EXAFS χ(k) function for uranium in (a) U(VI) in uranyl nitrate solution, (b) pure U film deposited from uranyl nitrate solution, "in-situ", (c) U(VI) + $Ni(OH)_2$ film, "in-situ", and (d) U(VI) + $Ni(OH)_2$ film, "ex-situ".

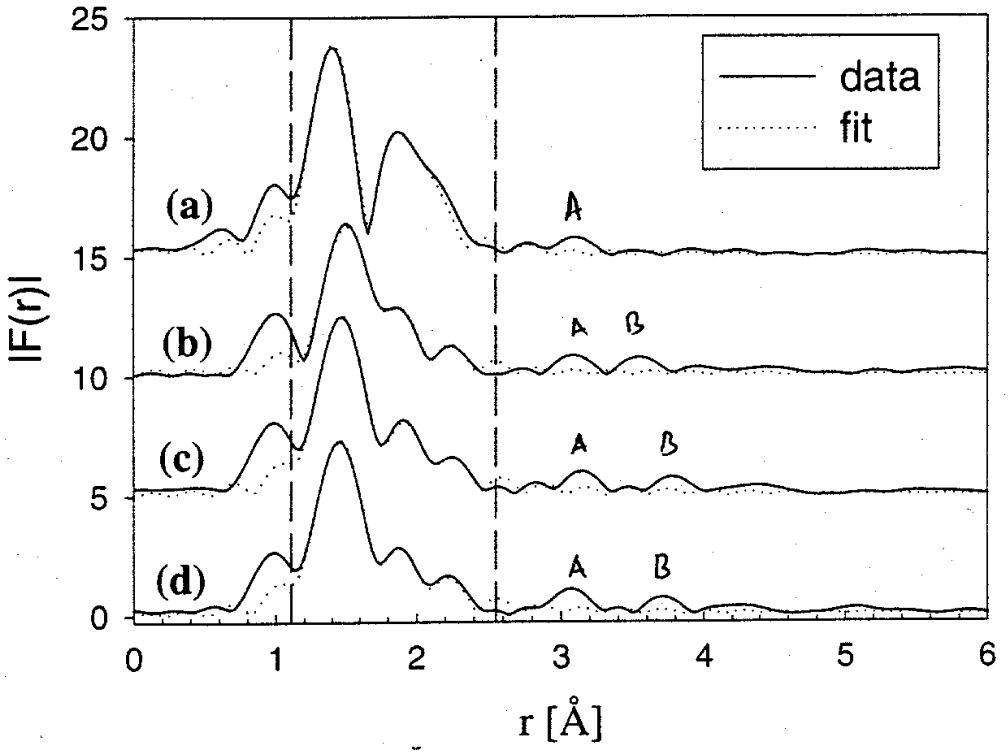

Figure 26. Fourier transforms corresponding to Fig. 25.